

# Multi-Partitioned Meshfree Quantum Finite Particle Method: A Hybrid Quantum Framework for Fluid Flow

Yudong Li<sup>1,2</sup>, Wenkui Shi<sup>1,2</sup>, Yan Li<sup>3,4</sup>, Chunfa Wang<sup>3,4</sup>,  
Ling Tao<sup>5</sup>, Zhuojia Fu<sup>6</sup>, Moubin Liu<sup>1,2,\*</sup>, Zhiqiang Feng<sup>3,4,7</sup>

1. School of Mechanics and Engineering Science, Peking University, Beijing 100871, PR China
2. Nanchang Institute of Innovation, Peking University, Nanchang 330038, PR China
3. School of Mechanics and Aerospace Engineering, Southwest Jiaotong University, Chengdu 611756, PR China
4. Advanced Structural Material Mechanics and Service Safety Key Laboratory of Sichuan Province, Chengdu 611756, PR China
5. School of Architecture and Civil Engineering, Xihua University, Chengdu 610039, PR China
6. College of Mechanics and Engineering Science, Hohai University, Nanjing 211100, PR China
7. Laboratory of Mechanics and Energy, Univ-Evry, Paris-Saclay University, Evry 91190, France

**Abstract** This study established a quantum-classical hybrid framework that integrates quantum computing paradigm with meshfree finite particle method. By harnessing quantum superposition and entanglement, it hybridized the critical computational kernels (termed as quantum finite particle method). A resource-efficient quantum computational strategy on multi-partitioned zones was proposed, which leverages a fixed small-scale quantum circuit as a fundamental processing unit to handle inner product for arbitrarily sized arrays. This approach employs iterative nesting of the quantum-core operation to accommodate varying input dimensions while maintaining hardware feasibility throughout. Motivated with developed quantum framework, the novel numerical discretization for hybrid quantum computational particle dynamics can be derived commonly and applied in fluid flows. Through a sequence of numerical experiments purposefully, the proposed numerical model was thoroughly validated and analyzed. Results demonstrate that integrating quantum computing to hybridize conventional linear combinations of particle dynamics serves as an effective high performance computing paradigm. By further extending into the numerical investigation of viscoelastic, highly elastic, and purely elastic fluids under high Weissenberg number conditions, the applicability of quantum-hybrid framework is significantly broadened. These advances provide critical insights facilitating the transition of quantum-enhanced fluid simulation toward practical engineering applications.

**Key words** Meshfree methods; Finite particle methods; Quantum computing paradigm; Enhanced multi-partitioned zones; Viscoelastic Weissenberg flows; Computational particle dynamics; Quantum processing unit

## 1 Introduction

Quantum computing has rapidly emerged as a transformative paradigm in computational science, heralding a new era where quantum mechanical phenomena on superposition and entanglement is harnessed to perform calculations that are infeasible for classical computers. This unique property enables quantum computers to process vast amounts of data in parallel, potentially offering exponential speedups for certain computational tasks, including matrix inversion, optimization, and simulation of quantum systems<sup>[1–3]</sup>. Paralleling to the advancements in quantum superposition and entanglement, the field of computational fluid dynamics (CFD) has generated significant progress on quantum fluid dynamics<sup>[4–6]</sup>. At present, some newish developments on meshfree computational particle dynamics and high performance computing (HPC) are being on the heels of quantum mechanical phenomena and crossed computing paradigms.

Mathematical models of computational fluid dynamics usually have intractable non-linear partial differential equations with a large of variables in two or higher dimensions, especially where the prevalent

---

\* Corresponding author. *E-mail address:* mbliu@pku.edu.cn (M.B. Liu).

neural networks are more likely to break out in higher-dimensional numerical problems<sup>[7]</sup>. Relatively comparing with classical numerical methods, as finite difference/element/volume methods and spectral Galerkin methods, quantum computing or quantum neural network has demonstrated astonishing computing potential<sup>[8]</sup>. Innovative scientific exploration is proceeding, as that Harrow-Hassidim-Lloyd (HHL) algorithm improved the computational ability on solving Navier-Stokes (NS) equations and even non-linear partial differential equations<sup>[9–11]</sup>, Todorova et al. built on the latter and presented the quantum lattice Boltzmann (LB) method between the LB streaming step and quantum walks<sup>[12]</sup>, and more efforts on Poisson equation solver by variational quantum algorithms (VQAs)<sup>[13]</sup> and quantum physics-informed neural networks (PINNs)<sup>[14]</sup> are developed.

Likewise with regard to classical meshfree methods, improved numerical strategies have been motivated to promote the computational precision, consistency and efficiency. These approaches mainly depend on the discretization of spatio-temporal variables and the numerical approximation on meshfree weak-strong forms<sup>[15–18]</sup>.

As a meshfree Lagrangian form, the smoothed particle hydrodynamics (SPH) is a particle-based method originally proposed by Gingold and Monaghan in 1977<sup>[19,20]</sup>. In early stages, the SPH technique did not receive significant attention compared with other well-established numerical methods, such as finite element, finite volume, and finite difference methods, that were already mature at the time. Although the SPH algorithm lacked the capability to conserve angular and linear momentum rigorously, it still produced results that were deemed acceptable for a variety of astrophysical applications. In contrast, when applied to problems in solid and fluid mechanics, the method encountered difficulties in accurately reproducing partial differential equations, particularly with respect to ensuring stability and achieving the desired level of accuracy. Subsequently, lacking and drawbacks were identified and improved by many researchers<sup>[21–23]</sup>. Improvements on the SPH method find its way to a wide range of applications<sup>[24]</sup>. Afterwards, the element free Galerkin (EFG) method<sup>[21,25]</sup> was emerged as a solution in earlier meshless techniques. It was specifically devised to mitigate issues such as diminished boundary accuracy and various instabilities, which were notably prevalent in SPH implementation. This approach was also named as the diffuse element method introduced by Nayroles et al.<sup>[26]</sup>. Kansa et al.<sup>[27]</sup> introduced the radial basis function (RBF) method as a means of addressing partial differential equations. Building upon this foundation, Fasshauer et al.<sup>[28]</sup> initially applied it to solve interpolation matrix problems and subsequently extended his research to enable the numerical resolution of partial differential equations. Certainly, considerable amount of meshless/meshfree methods was developed on different mathematical insights and intersectional processes. It spawned a lot of mathematical analysis and engineering applications<sup>[29–33]</sup>.

For the numerical approximation on meshfree methods, some means of linear combination, resolving matrices equation and time evolution are ubiquitous. With the enforcements on quantum superposition and quantum bits, these means can be of exponential acceleration by quantum computing. As a matter of course, the current consensus is that quantum physical devices will not simply supersede the classical high performance computing. Why is that? Firstly, the current noisy intermediate-scale quantum (NISQ)<sup>[34]</sup> device is not perfect enough to solve practical problems, but allows researchers to develop quantum algorithms and prepare for more advanced quantum hardware. Secondly, the specific quantum algorithms need to produce for different mathematics and engineering applications, existentially such as classical quantum phase estimation (QPE)<sup>[35]</sup>, Grover’s algorithm<sup>[36]</sup>, quantum walks<sup>[37]</sup>, Harrow-Hassidim-Lloyd (HHL) algorithm<sup>[38]</sup>, variational quantum algorithms (VQAs)<sup>[39]</sup>, etc. Thirdly, the present engineering building and application are both constructed based on central processing unit (CPU) chipset, accompanying with specified commands and special execution on graphics processing unit (GPU) chipset. Similarly, the interface on quantum processing unit (QPU) chipset is also facing great challenges, such as clock speed mismatch<sup>[40]</sup>, engineering quantum data encoding<sup>[41]</sup> and data interconnections<sup>[42]</sup>. As a fact, the present computing strategy is quantum-hybrid computer, both many parts of classical computation and key components by quantum processor.

As an improved weak-form collocation method, the finite particle method (FPM) has been extensively developed in fields of meshfree computational particle dynamics<sup>[43–46]</sup>, which was proposed based on the integral approximated scheme and the conception on multivariate mathematical Taylor series expansion<sup>[47]</sup>. Building upon the foundational residuals formulation in integral domains similarly as SPH methodology, several enhanced approaches have been developed to refine the FPM framework, supported by comprehensive numerical investigations<sup>[48–51]</sup>. By constructing residual bounds through moving least squares (MLS) and multivariate Taylor series expansion, the generalized finite difference method (GFDM) has also been adapted for applications in computational solid and fluid mechanics<sup>[52,53]</sup>. During the evolved procedure on numerical computation, the linear combination, resolving matrices equation and explicit/implicit integration usually take up most of the time and play the crucial role on general nu-

merical performance<sup>[2,54]</sup>. Yet, the computational burden of FPM escalates quickly as particle numbers and interaction complexity rise, making high-fidelity simulations of turbulent or multiphase flows particularly demanding<sup>[55]</sup>. The principles of quantum interference and entanglement further augment these capabilities. This paper investigates a quantum-classical hybrid framework that integrates quantum computing methodologies into the meshfree FPM simulation paradigm. By harnessing quantum superposition and entanglement, we improved critical computational kernels, overcoming the scalability constraints of conventional particle dynamics.

On the other hand, the extra elastic stress tensor in complex fluids, as a fundamental physical quantity in viscoelastic constitutive equations, evolves from the objective physical laws governing the modeled systems. Consequently, numerous nonlinear constitutive models were developed in early studies, including classical formulations such as Oldroyd-B, upper convected Maxwell (UCM), finite extensible nonlinear elastic (FENE), Phan-Thien-Tanner (PTT), and Giesekus models<sup>[56,57]</sup>. Notably, the nonlinear parameters presented in other models can be generally derived as extensions of the Oldroyd-B model, making it a benchmark for testing limits on numerical scheme stability. The UCM model represents a limiting case of Oldroyd-B, where their nonlinear elastic effects are governed by specific parameters  $(\alpha, \beta, \gamma)$ . Through parameter variation  $(\alpha \rightarrow 0, \beta \rightarrow 0, \gamma \rightarrow 0)$ , these characteristic models can degenerate into the Oldroyd-B formulation.

In the previous work<sup>[46]</sup>, we identified computational artifacts when directly applying time-dependent numerical discretization methods to the elastic UCM model. Two primary mechanisms underlie these instabilities: (a) Similar to dissipation in viscoelastic constitutive equations, the strain rate tensor diminishes with increasing relaxation time; (b) The conformation tensor inducing elastic stress cannot maintain symmetric positive definiteness (SPD) under arbitrary velocity gradient modifications. As established by Fattal, Kupferman et al.<sup>[58,59]</sup>, this numerical instability stems from an imbalance between exponential stress growth (originally from deformation) and convective transport, a phenomenon termed as the high Weissenberg number (HWN) problem<sup>[57]</sup>. Fattal et al.<sup>[60]</sup> pioneered the logarithmic conformation representation within finite element methods to resolve HWN challenges in viscoelastic flow simulations. Subsequent adaptations extended this approach to finite volume<sup>[61]</sup> and finite difference methods<sup>[62]</sup>, achieving stable simulations at Weissenberg numbers  $We \geq 10$ . In this paper, numerical analysis on high Weissenberg viscoelastic fluid flows is further investigated based on present hybrid quantum computing procedure. It is also to rigorously evaluate the HWN behaviors and improved meshfree numerical performance on accuracy and convergence. Through this paradigm, we demonstrated both methodological novelty and computational potential of the developed FPM framework and the quantum-hybridized implementation.

This paper is organized as follows: The fundamental quantum theory on swap test is described in Section 2; The proposed hybrid quantum framework on multi-partitioned meshfree quantum finite particle method is introduced in Section 3; The hybrid quantum computational particle dynamics involving common numerical discretization and viscoelastic Weissenberg fluid flows with Log conformation is described in Section 4; Some benchmarks of present hybrid quantum verification, valid time-dependent evolutionary flow states and numerical analysis on high Weissenberg viscoelastic fluid flows are proceeded orderly in Section 5; Some conclusions and remarks on present hybrid quantum resolution are given in Section 6.

## 2 Quantum theory: Swap test

To introduce a unified understanding of the distinctions between von Neumann computer and universal quantum computer, the operational principles  $|0\rangle, |1\rangle$  are described similarly from the expression on binary system. In classical computer architecture, the single bit 0, 1 can definitely describe the machine process of instruction order and data storage. While in universal quantum computer, the single quantum bit (qubit) is usually in a superposition state  $|\psi\rangle$ . The uncertain state can disappear (collapse) until that a definite result (observation) is executed. The property on uncertain superposition state can embody the potential parallel computing capability and data storage efficiency even combining with the entanglement effect of multiple quantum bits.

In order to facilitate the understanding on quantum system, the superposition state of single qubit can be described in Eq.(1) based on the Hilbert space. As shown in Fig.(1), the quantum superposition state can be quantized in the form of Bloch sphere. The state position is decided from the numerical amplitude and rotation angle, for which it notes that the state is still in an uncertain superposition state of probability amplitude. More mathematical details of quantum theory can be referenced<sup>[3,5,6]</sup>.

$$|\psi\rangle = \alpha |0\rangle + \beta |1\rangle \quad (1)$$

where  $\alpha, \beta$  denote the quantum amplitude  $\alpha, \beta \in \mathbb{C}$  and  $|\alpha|^2 + |\beta|^2 = 1$ .  $|0\rangle, |1\rangle$  denote a set of base space in  $\mathbb{C}^2$ ,  $|0\rangle = [1, 0]^T$  and  $|1\rangle = [0, 1]^T$ .

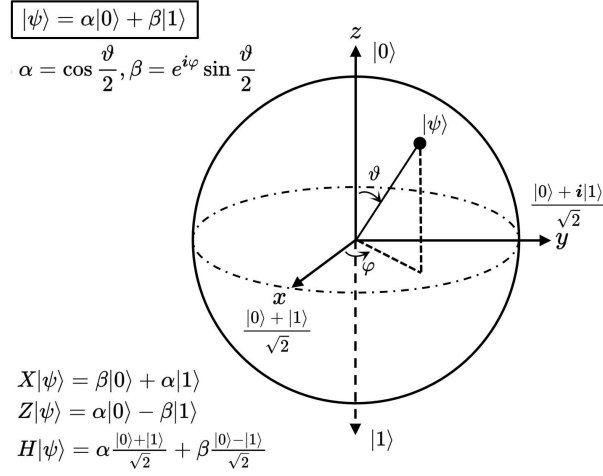


**Fig. 1** Bloch sphere of quantum state  $|\psi\rangle$  with basic gate operations.

**Quantum encoding:** Quantum state encoding maps classical data into quantum systems for computation. The primary methods<sup>[63,64]</sup> include:

- (a) Basis encoding by storing binary data directly in qubit states. It is simple but limited to discrete values.
- (b) Angle encoding by embedding data in qubit rotation angles. It is efficient for near-term quantum machine learning.
- (c) Amplitude encoding by encoding data into quantum amplitudes. It is highly compacted but requires complex preparation.
- (d) Hamiltonian encoding by encoding data into quantum system interactions. It is used in quantum simulation but sensitive to noise.

This study adopts the top-down amplitude encoding<sup>[64]</sup>, whose protocol operates through two phases: preprocessing the input vector to construct an angle tree representation, and then sequential encoding initiated from the root node. The implementation demonstrates the linear scaling in both circuit width  $O(\lceil \log_2 N \rceil)$  and circuit depth  $O(N)$ . The encoding example is displayed in Fig.(2).

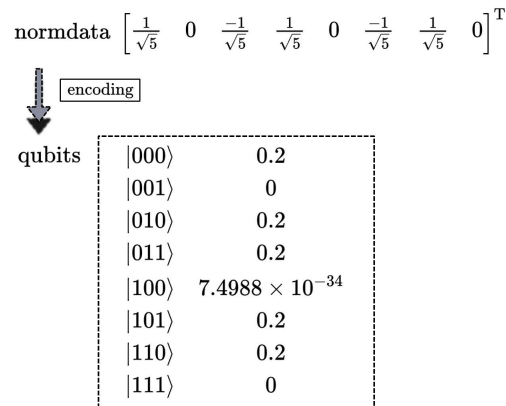


**Fig. 2** Amplitude encoding from normalized data array to quantum state.

The swap test is a quantum algorithm that estimates the overlap between two quantum states  $|u\rangle$  and  $|w\rangle$  by using an ancillary control qubit. The protocol involves preparing the ancilla in a superposition state, performing a controlled-swap operation between the target states, and measuring the ancilla to determine the state overlap  $|\langle u | w \rangle|^2$  from output probabilities. This method provides an efficient way to compare quantum states and evaluate their similarity, with applications ranging from quantum state characterization to machine learning, while requiring minimal quantum resources. However, its accuracy is inevitably limited by current noisy quantum hardware. The swap test method has been extensively

applied into fields on quantum computing<sup>[65,66]</sup>, which can promote the procedure on quantum inner product. Its quantum circuits usually include:

**Prepare the state:** In order to estimate the overlap between two quantum states  $|u\rangle$  and  $|w\rangle$  by swap test, the specified quantum state  $|\phi_p\rangle$  is prepared shown in Fig.(3). The  $U_u$  and  $U_w$  denote unitary transformation on quantum state encoding for  $|u\rangle$  and  $|w\rangle$ .

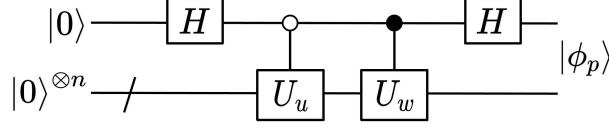


**Fig. 3** Quantum circuit to prepare the specified state  $|\phi_p\rangle$ .

$$|\phi_p\rangle = \frac{\sqrt{2}}{2} (|+\rangle |u\rangle + |-\rangle |w\rangle) \quad (2)$$

The state  $|\phi_p\rangle$  of Eq.(2) can be rewritten as

$$|\phi_p\rangle = \frac{1}{2} (|0\rangle (|u\rangle + |w\rangle) + |1\rangle (|u\rangle - |w\rangle)) \quad (3)$$

where the amplitude of  $|0\rangle$  is  $\sqrt{1 + \text{Re}\langle u | w \rangle} / \sqrt{2}$ , and the amplitude of  $|1\rangle$  is  $\sqrt{1 - \text{Re}\langle u | w \rangle} / \sqrt{2}$ .

Further, we conveniently represent  $|x\rangle$  and  $|y\rangle$  as the normalized states of  $|u\rangle + |w\rangle$  and  $|u\rangle - |w\rangle$ , respectively. Then there is a real number  $\theta_p \in [0, \pi/2]$  such that

$$|\phi_p\rangle = \sin \theta_p |0\rangle |x\rangle + \cos \theta_p |1\rangle |y\rangle \quad (4)$$

$$\begin{cases} \cos \theta_p = \sqrt{1 - \text{Re}\langle u | w \rangle} / \sqrt{2} \\ \sin \theta_p = \sqrt{1 + \text{Re}\langle u | w \rangle} / \sqrt{2} \end{cases} \quad (5)$$

$$\text{Re}\langle u | w \rangle = -\cos 2\theta_p \quad (6)$$

**Construct the unitary transformation:** Through preparing the specified state and the entanglement of two quantum states, the inner product can be embodied by their amplitude angle in Eq.(6). The present purpose is to calculate the  $\theta_p$  of Eq.(6) by quantum phase estimation algorithm. As a result, the specified constructed procedure on unitary transformation  $Q_p$  is implemented in Fig.(4).

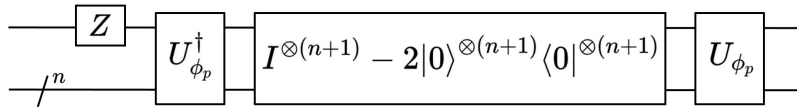


**Fig. 4** Construct the unitary transformation  $Q_p$ .

$$\begin{aligned} Q_p &= \left( I^{\otimes(n+1)} - 2|\phi_p\rangle\langle\phi_p| \right) (Z \otimes I^{\otimes n}) \\ &= U_{\phi_p} \left( I^{\otimes(n+1)} - 2|0\rangle^{\otimes(n+1)}\langle 0|^{\otimes(n+1)} \right) U_{\phi_p}^\dagger (Z \otimes I^{\otimes n}) \end{aligned} \quad (7)$$

where  $Z = |0\rangle\langle 0| - |1\rangle\langle 1|$  is the Pauli Z matrix.

As for the unitary operator  $I^{\otimes(n+1)} - 2|0\rangle^{\otimes(n+1)}\langle 0|^{\otimes(n+1)}$ , it flips the sign of the all-zero quantum state while leaving other states unchanged, acting as a key phase-based oracle in algorithms like Grover's search<sup>[36]</sup>. It can be implemented efficiently using controlled quantum gates despite operating on an exponentially large state space. We can run it in the circuit shown in Fig.(5)<sup>[67]</sup>.

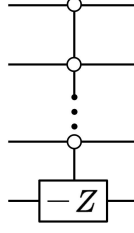


**Fig. 5** Quantum circuit of unitary operator  $I^{\otimes(n+1)} - 2|0\rangle^{\otimes(n+1)}\langle 0|^{\otimes(n+1)}$ .

Subsequently, Eq.(4) can be transformed by Schmidt decomposition method [68] as

$$\begin{aligned} |\phi_p\rangle &= \frac{-i}{\sqrt{2}} (e^{\theta_p i} |\zeta_+\rangle - e^{-\theta_p i} |\zeta_-\rangle) \\ |\zeta_{\pm}\rangle &= \frac{1}{\sqrt{2}} (|0\rangle |x\rangle \pm i |1\rangle |y\rangle) \end{aligned} \quad (8)$$

for the decomposed prepared state  $|\phi_p\rangle$ , the unitary transformation  $Q_p$  has the following characteristic equation as

$$Q_p |\zeta_{\pm}\rangle = e^{\pm 2\theta_p i} |\zeta_{\pm}\rangle \quad (9)$$

where  $|\zeta_{\pm}\rangle$  denotes the eigenstates of  $Q_p$ , the phase  $\theta_p$  is skillfully contained in the eigenvalues.

**Estimate the phase:** Currently adopt the quantum phase estimation (QPE) algorithm to estimate the phase  $\theta_p$ . The quantum circuit is shown in Fig.(6). During the procedure on quantum phase estimation, the circuit of auxiliary  $t$  qubits is constructed to estimate the phase  $\theta_p$  with higher precision, whose number of  $t$  qubits controls its calculation accuracy.

In Fig.(6), the FT indicates the quantum Fourier transform [69]. The control gate  $Q_p^k$  is composed with a series of controlled gates  $Q_p^{2^m}$  by ergodic  $m^{\text{th}}$  qubit in the first register as control qubit, where  $m = 0, \dots, t-1$ .

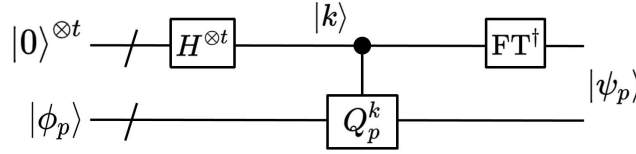


**Fig. 6** Estimate the proper phase  $\theta_p$  of unitary transformation  $Q_p$ .

The output state  $|\psi_p\rangle$  of quantum circuit by present algorithm can be described as

$$|\psi_p\rangle = \frac{-i}{\sqrt{2}} (e^{\theta_p i} |\lambda_e\rangle |\zeta_+\rangle - e^{-\theta_p i} |2^t - \lambda_e\rangle |\zeta_-\rangle) \quad (10)$$

where  $|\lambda_e\rangle$  denotes the auxiliary estimation state on  $t$  qubits, the binary value  $\lambda_e$  of maximum amplitude state has  $\lambda_e \in [0, 2^{t-1}]$  and then  $\lambda_e \pi / 2^t$  is the approximation on phase  $\theta_p$ .

Finally, combining with Eq.(6), the inner product has

$$\text{Re} \langle u | w \rangle \cong -\cos(\lambda_e \pi / 2^{t-1}) \quad (11)$$

Note that the imaginary part  $\text{Im} \langle u | w \rangle$  can be also estimated similarly in the quantum procedure of the real part of inner product. Given that the present study does not investigate the imaginary component solution of quantum computing, we will not elaborate further on this aspect [67].

### 3 Numerical approximation

#### 3.1 Meshfree finite particle method

As a comprehensive numerical scheme based on mathematical multivariate Taylor series expansion in Eq.(12), the meshfree finite particle method (FPM) considers a weighted discretization of weakly integral form described in Eq.(13).

$$f(\mathbf{x}) = f_i + f_{i,\alpha} (\mathbf{x}^\alpha - \mathbf{x}_i^\alpha) + O((\mathbf{x} - \mathbf{x}_i)^2) \quad (12)$$

$$\int_{\Omega} f(\mathbf{x}) \Phi(\mathbf{x} - \mathbf{x}_i) d\mathbf{x} = f_i \int_{\Omega} \Phi(\mathbf{x} - \mathbf{x}_i) d\mathbf{x} + f_{i,\alpha} \int_{\Omega} (\mathbf{x}^{\alpha} - \mathbf{x}_i^{\alpha}) \Phi(\mathbf{x} - \mathbf{x}_i) d\mathbf{x} + O((\mathbf{x} - \mathbf{x}_i)^2) \quad (13)$$

$$f_i = f(\mathbf{x}_i) \quad (14)$$

$$f_{i,\alpha} = f_{\alpha}(\mathbf{x}_i) = (\partial f / \partial \mathbf{x}^{\alpha})_i \quad (15)$$

$$\begin{bmatrix} \int_{\Omega} \omega(\mathbf{x} - \mathbf{x}_i) d\mathbf{x} & \int_{\Omega} (\mathbf{x}^{\alpha} - \mathbf{x}_i^{\alpha}) \omega(\mathbf{x} - \mathbf{x}_i) d\mathbf{x} \\ \int_{\Omega} \nabla \omega(\mathbf{x} - \mathbf{x}_i) d\mathbf{x} & \int_{\Omega} (\mathbf{x}^{\alpha} - \mathbf{x}_i^{\alpha}) \nabla \omega(\mathbf{x} - \mathbf{x}_i) d\mathbf{x} \end{bmatrix} \begin{bmatrix} f_i \\ f_{i,\alpha} \end{bmatrix} \cong \begin{bmatrix} \int_{\Omega} f(\mathbf{x}) \omega(\mathbf{x} - \mathbf{x}_i) d\mathbf{x} \\ \int_{\Omega} f(\mathbf{x}) \nabla \omega(\mathbf{x} - \mathbf{x}_i) d\mathbf{x} \end{bmatrix} \quad (16)$$

$$\mathbf{L} = \begin{bmatrix} \int_{\Omega} \omega(\mathbf{x} - \mathbf{x}_i) d\mathbf{x} & \int_{\Omega} (\mathbf{x}^{\alpha} - \mathbf{x}_i^{\alpha}) \omega(\mathbf{x} - \mathbf{x}_i) d\mathbf{x} \\ \int_{\Omega} \nabla \omega(\mathbf{x} - \mathbf{x}_i) d\mathbf{x} & \int_{\Omega} (\mathbf{x}^{\alpha} - \mathbf{x}_i^{\alpha}) \nabla \omega(\mathbf{x} - \mathbf{x}_i) d\mathbf{x} \end{bmatrix}, \mathbf{F} = \begin{bmatrix} f_i \\ f_{i,\alpha} \end{bmatrix}, \mathbf{B} = \begin{bmatrix} \int_{\Omega} f(\mathbf{x}) \omega(\mathbf{x} - \mathbf{x}_i) d\mathbf{x} \\ \int_{\Omega} f(\mathbf{x}) \nabla \omega(\mathbf{x} - \mathbf{x}_i) d\mathbf{x} \end{bmatrix} \quad (17)$$

where  $\Phi(\mathbf{x})$  represents a basis function defined within the support domain  $\Omega$ . Providing a set of basis functions  $\Phi(\mathbf{x}) = \{\omega^0(\mathbf{x}), \omega^1(\mathbf{x}), \omega^2(\mathbf{x}), \dots\}$  satisfies the corresponding consistency conditions on both sides of Eq.(12), a linear matrix system can be constructed using integrated kernel forms and purely physical discretized nodes. The choice of basis functions  $\omega^0(\mathbf{x}), \omega^1(\mathbf{x}), \omega^2(\mathbf{x}), \dots$  follows the approach proposed by Liu et al.<sup>[47]</sup>. Consequently, the smoothing function  $\omega(\mathbf{x})$  and its derivatives  $\nabla \omega(\mathbf{x})$  may serve as appropriate members of such a basis set. By employing distinct basis functions and omitting higher-order Taylor expansion terms, the linear matrix equation corresponding to Eq.(16) is derived.

By expressing the solution to the matrix Eq.(16) as  $\mathbf{F} \cong \mathbf{L}^{-1} \mathbf{B}$ , the finite particle method (FPM) is formally introduced. Neglecting the inversion of approximated functional value  $f_i$  leads to the kernel gradient correction (KGC) technique presented in Eq.(18), which can be also obtained through transformation of Eq.(13). In contrast to KGC, the FPM incorporates the resolved functional value  $f_i$  into the reorganized matrix system to achieve improved numerical accuracy.

$$\left[ \int_{\Omega} (\mathbf{x}^{\alpha} - \mathbf{x}_i^{\alpha}) \nabla \omega(\mathbf{x} - \mathbf{x}_i) d\mathbf{x} \right] [f_{i,\alpha}] \cong \left[ \int_{\Omega} (f(\mathbf{x}) - f_i) \nabla \omega(\mathbf{x} - \mathbf{x}_i) d\mathbf{x} \right] \quad (18)$$

In the case of smoothed particle hydrodynamics (SPH), the resolved matrix  $\mathbf{L}$  is commonly approximated as a unit matrix and neglected, allowing the physical variable to be directly approximated via Eq.(19) as a standard interpolation procedure. Although traditional SPH exhibits relatively low accuracy, it retains considerable numerical robustness, making it suitable for a wide range of practical engineering simulations<sup>[70]</sup>.

$$\begin{bmatrix} f_i \\ f_{i,\alpha} \end{bmatrix} \cong \begin{bmatrix} \int_{\Omega} f(\mathbf{x}) \omega(\mathbf{x} - \mathbf{x}_i) d\mathbf{x} \\ \int_{\Omega} f(\mathbf{x}) \nabla \omega(\mathbf{x} - \mathbf{x}_i) d\mathbf{x} \end{bmatrix} \quad (19)$$

Similarly, within the SPH framework, the approximations presented in Eq.(16) satisfy the properties required for constant functions, as specified in Eq.(20). By incorporating this condition, symmetric formulations of the aforementioned methods can be obtained for particle-particle interactions, as shown in Eqs.(21–23). These symmetric forms exhibit improved conservation properties in interactive dynamics.

$$\begin{bmatrix} \int_{\Omega} \omega(\mathbf{x} - \mathbf{x}_i) d\mathbf{x} & \int_{\Omega} (\mathbf{x}^{\alpha} - \mathbf{x}_i^{\alpha}) \omega(\mathbf{x} - \mathbf{x}_i) d\mathbf{x} \\ \int_{\Omega} \nabla \omega(\mathbf{x} - \mathbf{x}_i) d\mathbf{x} & \int_{\Omega} (\mathbf{x}^{\alpha} - \mathbf{x}_i^{\alpha}) \nabla \omega(\mathbf{x} - \mathbf{x}_i) d\mathbf{x} \end{bmatrix} \begin{bmatrix} \text{Const} \\ 0 \end{bmatrix} \cong \begin{bmatrix} \text{Const} \int_{\Omega} \omega(\mathbf{x} - \mathbf{x}_i) d\mathbf{x} \\ \text{Const} \int_{\Omega} \nabla \omega(\mathbf{x} - \mathbf{x}_i) d\mathbf{x} \end{bmatrix} \quad (20)$$

$$\text{FPM:} \begin{bmatrix} f_i \\ - \end{bmatrix} \cong \begin{bmatrix} \sum \omega_{ij} \Delta V_j & \sum \mathbf{x}_{ji}^{\beta} \omega_{ij} \Delta V_j \\ \sum \omega_{ij,\alpha} \Delta V_j & \sum \mathbf{x}_{ji}^{\alpha} \omega_{ij,\beta} \Delta V_j \end{bmatrix}^{-1} \begin{bmatrix} \sum f_j \omega_{ij} \Delta V_j \\ \sum f_j \omega_{ij,\beta} \Delta V_j \end{bmatrix} \quad (21)$$

$$\begin{bmatrix} - \\ f_{i,\alpha} \end{bmatrix} \cong \begin{bmatrix} \sum \omega_{ij} \Delta V_j & \sum \mathbf{x}_{ji}^{\beta} \omega_{ij} \Delta V_j \\ \sum \omega_{ij,\alpha} \Delta V_j & \sum \mathbf{x}_{ji}^{\alpha} \omega_{ij,\beta} \Delta V_j \end{bmatrix}^{-1} \begin{bmatrix} \sum (f_j - f_i) \omega_{ij} \Delta V_j \\ \sum (f_j - f_i) \omega_{ij,\beta} \Delta V_j \end{bmatrix} \quad (22)$$

$$\text{KGC: } [f_{i,\alpha}] \cong \left[ \sum \mathbf{x}_{ji}^{\alpha} \omega_{ij,\beta} \Delta V_j \right]^{-1} \left[ \sum (f_j - f_i) \omega_{ij,\beta} \Delta V_j \right] \quad (22)$$

$$\text{SPH: } f_i \cong \sum f_j \omega_{ij} \Delta V_j, \quad f_{i,\alpha} \cong \sum (f_j - f_i) \omega_{ij,\alpha} \Delta V_j \quad (23)$$

where the particle-particle interactional form is precisely as  $A_{ij} = A_i - A_j$ ,  $\omega_{ij,\beta}$  denotes the partial derivative of basis functional value and  $\Delta V_j$  denotes the volume of particle  $j$ .



### 3.2 Quantum finite particle method with multi-partitioned zones

According to the aforementioned quantum descriptions and numerical approximation on meshfree finite particle method, the hybrid quantum finite particle method (Q-FPM) is presented in this subsection. Based on the quantum phase estimation (QPE) on ancilla qubits, the complete quantum circuit diagram is described in Fig.(7), in which three qubits of norm data (the size of array is  $2^n$ ,  $n$  is the size of qubits of norm data) and four ancilla qubits ( $t = 4$ ) for observation are requested. Quantum results on QPE measurement are counted and concluded by a large number of quantum observations (quantum collapse). The procedure is to find the specific quantum superposition state that has been observed at the most times.

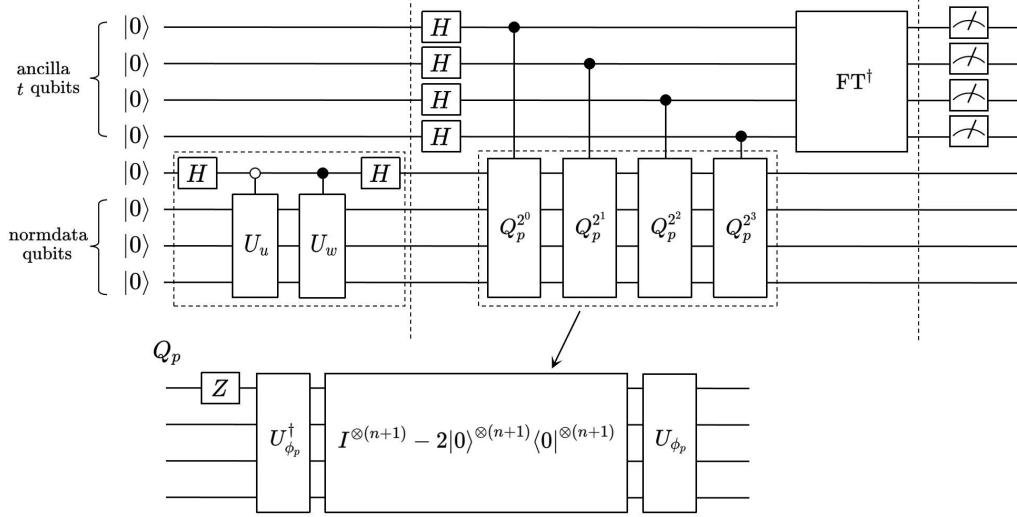


**Fig. 7** Complete quantum circuit diagram in quantum finite particle method.

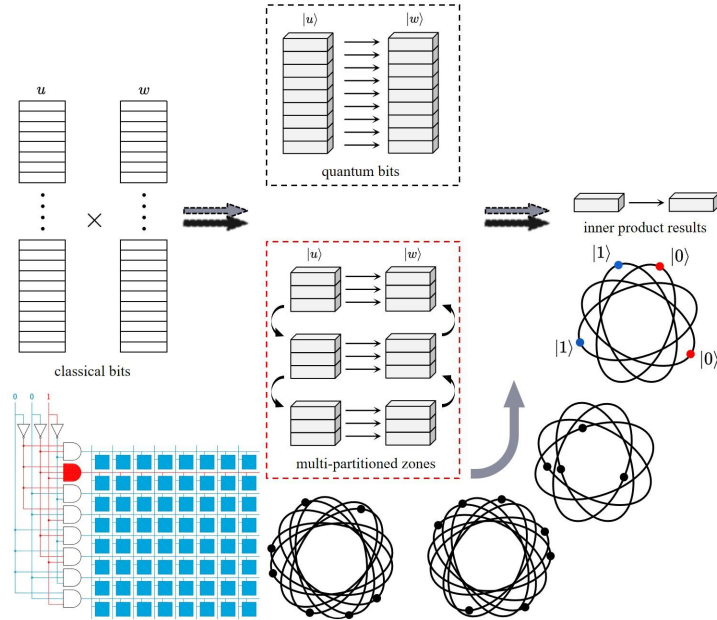


**Fig. 8** The fixed small-scale quantum procedure on advantaged multi-partitioned zones.

In Eqs.(21-23) of meshfree numerical approximation, the superimposed form array of adjacent summation is usually the changeable structure and of a large scale for general computational particle methods. Further considering the indefinite requests on computing size of qubits and the current limitation on NISQ device, this study proposed the strategy of multi-partitioned zones to optimize the requests on qubits and improve the efficiency on quantum computing. As shown in Fig.(8), the classical  $N$  bits of



data arrays are requested on the form of binary system and the quantum bits  $n = \log(N)$  are requested accordingly. The resource-efficient quantum computational strategy on multi-partitioned zones leverages a fixed small-scale quantum circuit as a fundamental processing unit, which is iteratively nested to handle inner product calculations for arbitrarily sized arrays described in Eq.(24). Hence the quantum finite particle method with multi-partitioned zones is more suitable to perform an inner product process of indefinite scales in the current quantum device.

Through the hybrid quantum finite particle method and the representation on corresponding quantum circuits, the quantum approximation can be transformed in Eqs.(25-27) based on the meshfree particle approximation on Eqs.(21-23). Following the Eq.(11) and Eq.(24),  $\langle u_j | w_j \rangle_{j=1,2,\dots}$  denotes the quantum inner product calculations for arbitrarily sized arrays ( $j = 1, 2, \dots$ ). In this form, the meshfree numerical approximation can be represented as the quantum structure of neighboring particle cluster. Therein, the special smoothing kernel  $\omega_{ij}$  and its derivatives  $\omega_{ij,\alpha}$  are locally weighted and constructed as the right product state. The superscript  $c$  denotes the kernel correction on FPM scheme and the definition on spatial dimension ( $\alpha, \beta = 0, x, y, z$ ) contributes the approximation on original function value and spatial directional discretization, where the KGC neglected the inversion on approximated functional value  $f_i$  and is only related with the discretization on spatial direction. In this study, smoothing kernel functions are requested and described detailedly in the previous work [45, 70].

$$u \cdot w = u_j w_j \cong \langle u | w \rangle_{j=1,2,\dots} \quad (24)$$

$$\text{FPM:} \begin{cases} f_i \cong \langle f_j \Delta V_j | \omega_{ij,\alpha=0}^c \rangle_{j=1,2,\dots} \\ f_{i,\alpha} \cong \langle (f_j - f_i) \Delta V_j | \omega_{ij,\alpha}^c \rangle_{j=1,2,\dots} \\ \omega_{ij,\alpha}^c \cong \left\langle [L_i^{\alpha\beta}]^{-1} | \omega_{ij,\beta} \right\rangle_{\beta=0,x,y,z} \\ [L_i^{\alpha\beta}] \cong \langle x_{ji}^\alpha \Delta V_j | \omega_{ij,\beta} \rangle_{j=1,2,\dots} \end{cases} \quad (25)$$

$$\text{KGC:} \begin{cases} f_{i,\alpha} \cong \langle (f_j - f_i) \Delta V_j | \omega_{ij,\alpha}^c \rangle_{j=1,2,\dots} \\ \omega_{ij,\alpha}^c \cong \left\langle [L_i^{\alpha\beta}]^{-1} | \omega_{ij,\beta} \right\rangle_{\beta=x,y,z} \\ [L_i^{\alpha\beta}] \cong \langle x_{ji}^\alpha \Delta V_j | \omega_{ij,\beta} \rangle_{j=1,2,\dots} \end{cases} \quad (26)$$

$$\text{SPH:} \begin{cases} f_i \cong \langle f_j \Delta V_j | \omega_{ij} \rangle_{j=1,2,\dots} \\ f_{i,\alpha} \cong \langle (f_j - f_i) \Delta V_j | \omega_{ij,\alpha} \rangle_{j=1,2,\dots} \end{cases} \quad (27)$$

## 4 Hybrid quantum computational particle dynamics

In computational particle dynamics, the numerical discretization of physical variables can be formulated within meshfree frameworks. Building upon the developed quantum inner product strategy, this study introduces a novel discretization approach tailored for hybrid quantum computational particle dynamics. Specifically, Eq.(28) discretizes the divergence of fluid velocity, Eq.(29) provides a gradient discretization accounting for variable density, and Eq.(30) approximates the Laplace operator via finite differences likely for second-order derivatives [71], which may be also represented by nested summation. Furthermore, Eq.(31) presents a finite-difference-type formulation integrated with the proposed hybrid quantum procedure.

$$\nabla \cdot \mathbf{v}_i \cong \left\langle \frac{m_j}{\rho_j} \left| \left\langle v_{ji}^\beta | \omega_{ij,\beta}^c \right\rangle_{\beta=x,y,z} \right\rangle_{j=1,2,\dots,N} \quad (28)$$

$$\frac{1}{\rho_i} \nabla f_i \cong \left\langle m_j \left( \frac{f_i}{\rho_i^2} + \frac{f_j}{\rho_j^2} \right) \left| \nabla \omega_{ij}^c \right\rangle_{j=1,2,\dots,N} \quad (29)$$

$$\nabla^2 f_i \cong \left\langle \frac{4f_{ij}m_j}{(\rho_i + \rho_j)(r_{ij}^2)} \left| \left\langle r_{ij}^\beta | \omega_{ij,\beta}^c \right\rangle_{\beta=x,y,z} \right\rangle_{j=1,2,\dots,N} \quad (30)$$

$$\begin{cases}
f_{i,\beta} \cong \left\langle \frac{2f_{ji}m_j}{(\rho_i+\rho_j)} \left| \omega_{ij,\beta}^c \right\rangle_{j=1,2,\dots,N} \\
f'_{i,\beta} \cong \frac{f'_j - f'_i}{r_{ji}^\beta} = \frac{f'_{ji} - f'_{ij}}{r_{ji}^\beta} = \frac{2f'_{ij}}{r_{ij}^\beta} \\
\nabla^2 f_i = \nabla \cdot \nabla f_i \cong \left\langle 2f'_{ij} \left| \frac{1}{r_{ij}^\beta} \right\rangle_{j=1,2,\dots,N} \cong \left\langle \frac{4f_{ji}m_j}{(\rho_i+\rho_j)} \left| \left\langle \frac{1}{r_{ij}^\beta} \left| \omega_{ij,\beta}^c \right\rangle_{\beta=x,y,z} \right\rangle_{j=1,2,\dots,N} \right. \right. \\
\cong - \left\langle \frac{4f_{ji}m_j}{(\rho_i+\rho_j)} \left| \left\langle \frac{r_{ij}^\beta}{(r_{ij}^2)} \left| \omega_{ij,\beta}^c \right\rangle_{\beta=x,y,z} \right\rangle_{j=1,2,\dots,N} \cong \left\langle \frac{4f_{ij}m_j}{(\rho_i+\rho_j)(r_{ij}^2)} \left| \left\langle r_{ij}^\beta \left| \omega_{ij,\beta}^c \right\rangle_{\beta=x,y,z} \right\rangle_{j=1,2,\dots,N}
\end{cases} \quad (31)$$

where  $N$  denotes the number of surrounding neighboring particles  $j$  at source particle  $i$ .  $m_j$ ,  $\rho_j$  denote the mass and density of particle  $j$  respectively,  $f_i$  denotes the approximated physical variable,  $\mathbf{v}_i$  denotes the general velocity and  $\omega_{ij,\beta}^c$  denotes the first-order derivative on approximated kernels derived by aforementioned quantum schemes. Note that  $\langle \cdot \rangle_{j=1,2,\dots}$  denotes the aforementioned quantum-hybrid numerical implementation.

#### 4.1 Numerical discretization on computational fluid equations

Based on the Navier Stokes framework, the complete governing equations for viscoelastic fluid flow are presented in Eqs.(32–37). These include the continuity Eq.(32), the momentum Eq.(33), and an independent constitutive relation for Oldroyd-B viscoelasticity in Eq.(35).

$$\frac{d\rho}{dt} = -\rho \nabla \cdot \mathbf{v} \quad (32)$$

$$\frac{d\mathbf{v}}{dt} = \frac{1}{\rho} \nabla \cdot \hat{\boldsymbol{\sigma}} + \mathbf{g} \quad (33)$$

$$\hat{\boldsymbol{\sigma}} = -p\hat{\mathbf{I}} + \hat{\boldsymbol{\tau}}_s + \vartheta \hat{\boldsymbol{\tau}}_p \quad (34)$$

$$\hat{\boldsymbol{\tau}}_p + \lambda_1 \overset{\nabla}{\hat{\boldsymbol{\tau}}_p} = \mu_p \left( \nabla \mathbf{v} + (\nabla \mathbf{v})^T \right) \quad (35)$$

$$\overset{\nabla}{\hat{\boldsymbol{\tau}}_p} = \frac{d\hat{\boldsymbol{\tau}}_p}{dt} - \hat{\boldsymbol{\tau}}_p \cdot (\nabla \mathbf{v}) - (\nabla \mathbf{v})^T \cdot \hat{\boldsymbol{\tau}}_p \quad (36)$$

$$\frac{d\hat{\boldsymbol{\tau}}_p}{dt} = \hat{\boldsymbol{\tau}}_p \cdot (\nabla \mathbf{v}) + (\nabla \mathbf{v})^T \cdot \hat{\boldsymbol{\tau}}_p - \frac{1}{\lambda_1} \hat{\boldsymbol{\tau}}_p + \frac{\mu_p}{\lambda_1} \left( \nabla \mathbf{v} + (\nabla \mathbf{v})^T \right) \quad (37)$$

Building upon the numerical discretization established for the quantum computational particle dynamics approach and integrating the weakly compressible smoothed particle hydrodynamics (WCSPH) framework<sup>[49]</sup>, the corresponding particle–particle interaction formulations can be derived as follows:

$$\left( \frac{d\rho}{dt} \right)_i \cong \left\langle \frac{m_j \rho_i}{\rho_j} \left| \left\langle v_{ij}^\beta \left| \omega_{ij,\beta}^c \right\rangle_{\beta=x,y,z} \right\rangle_{j=1,2,\dots,N} \right. \quad (38)$$

$$\left( \frac{dv^\alpha}{dt} \right)_i \cong \left\langle m_j \left| \left\langle \left( \frac{\sigma_i^{\alpha\beta}}{\rho_i^2} + \frac{\sigma_j^{\alpha\beta}}{\rho_j^2} \right) \left| \omega_{ij,\beta}^c \right\rangle_{\beta=x,y,z} \right\rangle_{j=1,2,\dots,N} - \left\langle m_j \left| \left\langle \Pi_{ij} \delta^{\alpha\beta} \left| \omega_{ij,\beta}^c \right\rangle_{\beta=x,y,z} \right\rangle_{j=1,2,\dots,N} + g_i^\alpha \right. \quad (39)$$

$$\sigma_i^{\alpha\beta} = -p_i \delta^{\alpha\beta} + \mu_s \left( k_i^{\alpha\beta} + k_i^{\beta\alpha} \right) + \vartheta \cdot \tau_{pi}^{\alpha\beta} \quad (40)$$

$$p_i = \frac{\rho_0 c^2}{\gamma} \left( \left( \frac{\rho_i}{\rho_0} \right)^\gamma - 1 \right) \quad (41)$$

$$\left( \frac{d\tau_p^{\alpha\beta}}{dt} \right)_i \cong k_i^{\alpha\gamma} \tau_{pi}^{\gamma\beta} + k_i^{\beta\gamma} \tau_{pi}^{\gamma\alpha} - \frac{1}{\lambda_1} \tau_{pi}^{\alpha\beta} + \frac{\mu_p}{\lambda_1} \left( k_i^{\alpha\beta} + k_i^{\beta\alpha} \right) \quad (42)$$

$$k_i^{\alpha\beta} = \left( \frac{\partial v^\alpha}{\partial x^\beta} \right)_i \cong \left\langle v_{ji}^\alpha \frac{m_j}{\rho_j} \left| \omega_{ij,\beta}^c \right\rangle_{j=1,2,\dots,N} \quad (43)$$

The fluid stress  $\sigma_i^{\alpha\beta}$  comprises from isotropic pressure  $p_i$ , solvent viscous stress  $\tau_{si}^{\alpha\beta}$ , and polymeric elastic stress  $\tau_{pi}^{\alpha\beta}$ . The constitutive model is adjusted by the numerical factor  $\vartheta$ . Solvent and polymeric contributions are characterized by viscosities  $\mu_s$  and  $\mu_p$ , respectively, while  $\lambda_1$  represents the relaxation

time of viscoelastic fluid. Gravitational acceleration is incorporated via the spatial vector  $g_i^\alpha$ . The equation of state in Eq.(41) models the isotropic pressure, where  $\rho_0$  is the reference density,  $\gamma = 7$  is a constant, and  $c$  denotes the speed of sound, typically an order of magnitude greater than the characteristic velocity.

In hydrodynamic simulations, the absence of dissipative terms in the momentum equation often leads to significant numerical oscillations. To mitigate such instabilities particularly in highly deformable flows and shock-induced dissipation, the artificial viscosity models were introduced by Monaghan et al. [20]. In contrast to low-Reynolds-number viscous flows, the artificial viscosity formulation in Eq.(44) employs parameters  $\alpha_\Pi = 0.01$ ,  $\beta_\Pi = 2.0$  for Newtonian fluids and  $\alpha_\Pi = 1.0$ ,  $\beta_\Pi = 2.0$  for viscoelastic non-Newtonian fluids, accounting for physical viscosity through nested summation. A widely adopted form integrated with hybrid quantum computing is implemented as follows:

$$\Pi_{ij} = \begin{cases} \frac{-\alpha_\Pi \bar{c}_{ij} \phi_{ij} + \beta_\Pi \phi_{ij}^2}{\bar{\rho}_{ij}}, \langle v_{ij}^\alpha | r_{ij}^\alpha \rangle_{\alpha=x,y,z} < 0 \\ 0, \langle v_{ij}^\alpha | r_{ij}^\alpha \rangle_{\alpha=x,y,z} \geq 0 \end{cases} \quad (44)$$

$$\phi_{ij} = \frac{h \langle v_{ij}^\alpha | r_{ij}^\alpha \rangle_{\alpha=x,y,z}}{r_{ij}^2 + 0.01 h^2} \quad (45)$$

$$\bar{c}_{ij} = (c_i + c_j)/2, \bar{\rho}_{ij} = (\rho_i + \rho_j)/2 \quad (46)$$

Employing the weakly compressible SPH framework and assuming approximate incompressibility ( $\nabla \cdot \mathbf{v} \approx 0$ ), the momentum equation given in Eq.(33) can be reformulated as Eq.(47). This reformulation corresponds to an alternative numerical approach in which the viscous term is discretized in a finite-difference-like form within the SPH context [71]. This technique effectively suppresses numerical oscillations while preserving the physical fidelity of solvent viscosity in both Newtonian and viscoelastic non-Newtonian fluid flows.

$$\frac{d\mathbf{v}}{dt} = -\frac{1}{\rho} \nabla p + \frac{\mu_s}{\rho} \nabla^2 \mathbf{v} + \frac{\vartheta}{\rho} \nabla \cdot \hat{\boldsymbol{\tau}}_p + \mathbf{g} \quad (47)$$

$$\begin{aligned} \left( \frac{dv^\alpha}{dt} \right)_i &\cong - \left\langle m_j \left( \frac{p_i}{\rho_i^2} + \frac{p_j}{\rho_j^2} \right) | \omega_{ij,\alpha}^c \right\rangle_{j=1,2,\dots,N} + \left\langle \frac{4(\mu_{si} + \mu_{sj}) m_j v_{ij}^\alpha}{(\rho_i + \rho_j)^2 (r_{ij}^2 + 0.01 h^2)} \left| \left\langle r_{ij}^\beta | \omega_{ij,\beta}^c \right\rangle_{\beta=x,y,z} \right\rangle_{j=1,2,\dots,N} \right. \\ &\quad \left. + \left\langle \vartheta m_j \left| \left\langle \left( \frac{\tau_{pi}^{\alpha\beta}}{\rho_i^2} + \frac{\tau_{pj}^{\alpha\beta}}{\rho_j^2} \right) | \omega_{ij,\beta}^c \right\rangle_{\beta=x,y,z} \right\rangle_{j=1,2,\dots,N} \right. + g_i^\alpha \end{aligned} \quad (48)$$

where Eq.(48) denotes the hybrid quantum FPM form on finite-difference-like formula for viscosity diffusion term.  $r_{ij}$  denotes the spatial distance between particle  $i$  and particle  $j$ , and  $h$  denotes the smoothing kernel length. For the simulations performed in this study, the density variation can be controlled to be within 0.01 to maintain a nearly constant density.

## 4.2 High Weissenberg number and Log conformation

In the numerical implementation of time-dependent constitutive equations particularly for purely elastic upper convected Maxwell (UCM) models, explicit numerical integration in Eq.(42) often encounters the high Weissenberg number (HWN) problem under critical conditions. In reality, this instability arises from the loss of symmetric positive definite (SPD) properties in the conformation tensor during the computational procedure on high Weissenberg number. The explicit integration process cannot effectively preserve the SPD properties. This fundamental limitation explains why that traditional stabilization techniques ultimately fail beyond certain Weissenberg thresholds, necessitating alternative approaches like Log-conformation representations to maintain both stability and physical fidelity in viscoelastic flow simulations.

As previously discussed, the viscoelastic stress is governed by the strain function and conformation tensor in Eq.(49). The conformation tensor  $\hat{\mathbf{A}}$  provides a macroscopic representation of the average orientation of polymer chains and inherently satisfies SPD property. By substituting Eq.(49) into the constitutive model of Eq.(35), the time evolution of conformation tensor is expressed as Eq.(50), where Eq.(51) defines its upper-convected derivative.

$$\hat{\boldsymbol{\tau}}_p = \frac{\mu_p}{\lambda_1} (\hat{\mathbf{A}} - \hat{\mathbf{I}}) \quad (49)$$

$$\overset{\nabla}{\hat{\mathbf{A}}} = -\frac{1}{\lambda_1}(\hat{\mathbf{A}} - \hat{\mathbf{I}}) \quad (50)$$

$$\overset{\nabla}{\hat{\mathbf{A}}} = \frac{d\hat{\mathbf{A}}}{dt} - \hat{\mathbf{A}} \cdot (\nabla \mathbf{v})^T - (\nabla \mathbf{v}) \cdot \hat{\mathbf{A}} \quad (51)$$

Here, the upper-convected derivative ensures the frame invariance for both material deformation and rotational effects. By extracting the symmetric positive definite (SPD) conformation tensor from the constitutive formulation and coupling it with an improved particle discretization scheme, the SPD property can be rigorously maintained, thereby resolving the high Weissenberg number problem. The logarithmic representation of conformation tensor  $\hat{\Psi} = \log(\hat{\mathbf{A}})$  is introduced and mathematically expressed as follows:

$$\hat{\mathbf{A}} = \hat{\mathbf{E}} \hat{\Lambda} \hat{\mathbf{E}}^T \quad (52)$$

$$\hat{\Psi} = \hat{\mathbf{E}} \log(\hat{\Lambda}) \hat{\mathbf{E}}^T \quad (53)$$

where  $\hat{\mathbf{E}}$  and  $\hat{\Lambda}$  denote the eigenvector matrix and eigenvalue matrix, respectively. The SPD tensor can be completely represented by its spectral decomposition and the logarithmic transformation must be constrained to non-zero components for preventing singularities.

The velocity gradient tensor  $\nabla \mathbf{v}$  can be decomposed into three fundamental components: a traceless symmetric extension component, a commutation tensor and an antisymmetric pure rotation tensor, as follows:

$$\nabla \mathbf{v} = \hat{\Omega} + \hat{\mathbf{B}} + \hat{\mathbf{N}} \hat{\mathbf{A}}^{-1} \quad (54)$$

$$\hat{\mathbf{E}}^T \nabla \mathbf{v} \hat{\mathbf{E}} = \hat{\mathbf{E}}^T \hat{\Omega} \hat{\mathbf{E}} + \hat{\mathbf{E}}^T \hat{\mathbf{B}} \hat{\mathbf{E}} + \hat{\mathbf{N}} \hat{\Lambda}^{-1} \quad (55)$$

$$\begin{bmatrix} m_{11} & m_{12} & m_{13} \\ m_{21} & m_{22} & m_{23} \\ m_{31} & m_{32} & m_{33} \end{bmatrix} = \hat{\mathbf{E}}^T \nabla \mathbf{v} \hat{\mathbf{E}}, \hat{\Omega} = \hat{\mathbf{E}} \begin{bmatrix} 0 & \omega_{12} & \omega_{13} \\ -\omega_{12} & 0 & \omega_{23} \\ -\omega_{13} & -\omega_{23} & 0 \end{bmatrix} \hat{\mathbf{E}}^T, \hat{\mathbf{B}} = \hat{\mathbf{E}} \begin{bmatrix} m_{11} & 0 & 0 \\ 0 & m_{22} & 0 \\ 0 & 0 & m_{33} \end{bmatrix} \hat{\mathbf{E}}^T \quad (56)$$

$$\omega_{12} = \frac{\lambda_2 m_{12} + \lambda_1 m_{21}}{\lambda_2 - \lambda_1}, \omega_{13} = \frac{\lambda_3 m_{13} + \lambda_1 m_{31}}{\lambda_3 - \lambda_1}, \omega_{23} = \frac{\lambda_3 m_{23} + \lambda_2 m_{32}}{\lambda_3 - \lambda_2} \quad (57)$$

where the tensors  $\hat{\mathbf{B}}$ ,  $\hat{\Omega}$ , and  $\hat{\mathbf{N}}$  represent a symmetric matrix and two antisymmetric matrices, respectively. This numerical relationship can be characterized by the definition in Eq.(54). Note that the matrix  $\hat{\mathbf{N}}$  vanishes in subsequent derivative derivations and is therefore omitted. For the computed eigenvalues of SPD tensor  $\hat{\mathbf{A}}$ , uniqueness and distinctness are guaranteed in three-dimensional space.

During the subsequent time integration process, the key objective is to decompose the velocity gradient to preserve the SPD property. By substituting Eq.(54) into Eq.(50) and Eq.(51), we obtained the reformulated expression given in Eq.(58). Further introducing the logarithmic transformation of conformation tensor, the log-conformation representation can be described in Eq.(59).

$$\frac{d\hat{\mathbf{A}}}{dt} = \hat{\Omega} \hat{\mathbf{A}} - \hat{\mathbf{A}} \hat{\Omega} + \hat{\mathbf{B}} \hat{\mathbf{A}} + \hat{\mathbf{A}} \hat{\mathbf{B}} - \frac{1}{\lambda_1} f_R(\hat{\mathbf{A}}) \quad (58)$$

$$\frac{d\hat{\Psi}}{dt} = \hat{\Omega} \hat{\Psi} - \hat{\Psi} \hat{\Omega} + 2\hat{\mathbf{B}} - \frac{1}{\lambda_1} e^{-\hat{\Psi}} f_R(e^{\hat{\Psi}}) \quad (59)$$

Therefore, Eq.(59) describes the evolution of the SPD property in the Log-conformation formulation. Compared to direct computation via Eq.(37), this transformation leverages the intrinsic properties of symmetric matrices to rigorously maintain SPD characteristics throughout iterative computations.

To distinguish advection, source terms, and maintain stable SPD properties during numerical integration, a time-splitting numerical scheme<sup>[57]</sup> is adopted for polymer stress tensor integration, as follows:

$$\left( \frac{d\mathbf{A}}{dt} \right)_i^{\alpha\beta} = \Omega_i^{\alpha\gamma} A_i^{\gamma\beta} - A_i^{\alpha\gamma} \Omega_i^{\gamma\beta} + B_i^{\alpha\gamma} A_i^{\gamma\beta} + A_i^{\alpha\gamma} B_i^{\gamma\beta} \quad (60)$$

$$\left( \frac{d\mathbf{A}}{dt} \right)_i^{\alpha\beta} = -\frac{1}{\lambda_1} f_R(A_i^{\alpha\beta}) \quad (61)$$

$$\left( \frac{d\Psi}{dt} \right)_i^{\alpha\beta} = \Omega_i^{\alpha\gamma} \Psi_i^{\gamma\beta} - \Psi_i^{\alpha\gamma} \Omega_i^{\gamma\beta} + 2B_i^{\alpha\beta} \quad (62)$$

$$\left( \frac{d\Psi}{dt} \right)_i^{\alpha\beta} = -\frac{1}{\lambda_1} e^{-\Psi_i^{\alpha\beta}} f_R(e^{\Psi_i^{\alpha\beta}}) \quad (63)$$

### 4.3 Time integration and other technologies

During this hybrid procedure on meshfree computational particle dynamics and quantum computing, the classical time integration on explicit propulsion and other technologies of boundary treatment, etc. are adopted in the present study to ensure the effectiveness and continuity of dynamic computing process shown in Fig.(9). Therein, the time evolutionary treatment, predictor-corrector Symplectic scheme is introduced, whose time step has the second-order accuracy to calculate independent physical variables. Specific details on some necessary numerical technologies have been introduced in literatures [45, 46, 48, 49, 55]. As this aspect falls outside the main scope of present work, it will not be elaborated further apologetically.

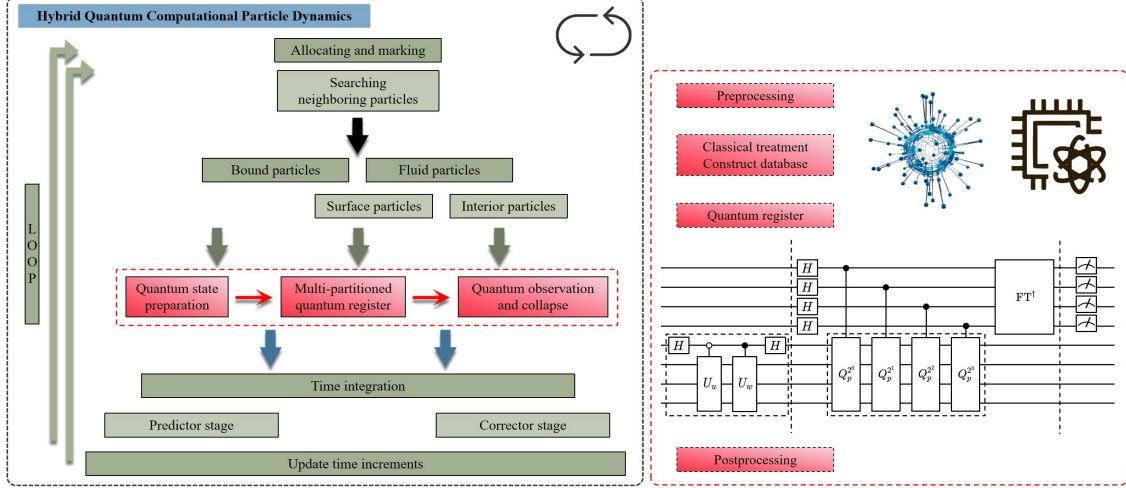


Fig. 9 Thematic concept on hybrid quantum computational particle dynamics.

## 5 Numerical simulation

Considering the current limitation on noisy intermediate-scale quantum (NISQ) device, we mainly adopted the quantum algorithm based on classical computer such as Qiskit from IBM, whose quantum assembly instruction can be same and suitable with the quantum hardware. It is entirely demonstrated that the distinction of final results merely stems from hardware devices between von Neumann computer and universal quantum computer with noise [5]. The relative norm error evaluations are adopted in these numerical investigations shown in Eq.(64).

$$E_2 = \sqrt{\sum_i^N (f_i^{numerical} - f_i^{analytical})^2} / \sqrt{\sum_i^N (f_i^{analytical})^2} \quad (64)$$

### Case 1: Hybrid quantum verification on statical exact solution

In this subsection, the valid verification on present hybrid quantum FPM with statical exact solution is proceeded purposefully. We introduced a simple function of Eq.(65) and gradually a complicated function of Eq.(66) with multi-curvature changing. It adopts orthogonal particle distributions and the first-order partial derivative of gradient  $\nabla F$  and second-order partial derivative of Laplace  $\nabla^2 F$  are numerically investigated.

Based on the numerical approximation on Eq.(65), Fig.(10) described the approximation on first-order partial derivative by the entire meshfree particle computing, hybrid quantum computing and global quantum computing with multi-partitioned zones. The corresponding relative errors of quantified nodes are calculated shown in Table 1. The integrated FPM approximation is superior to traditional SPH on computational accuracy, whose conclusion had been demonstrated comprehensively [48, 49, 70]. However, quantum-hybrid meshfree algorithms offer theoretical advantages and exploratory prospects. Their current implementation fidelity (typically < 99.9% for NISQ-era processors) imposes unavoidable accuracy reductions of approximately  $10^{-4} \sim 10^{-3}$  compared to classical meshfree solutions (error  $10^{-7} \sim 10^{-6}$ ). The fidelity estimation is also subject to errors induced by matrix inversion. The Q-FPM represents the hybrid quantum kernel procedure shown in Eq.(25), which usually involves small size computation

of inner product at each particle. Further the quantum procedure on particle dynamics is constructed based on the linear combination of surrounding neighboring particles with arbitrarily sized arrays and GQ-FPM represents the global hybrid quantum procedure with automatic multi-partitioned zones shown in Eqs.(28-30) and Figs.(7-8). Inevitably the accuracy of fidelity computation is reduced approximately  $10^{-1}$  from quantum kernel to quantum particle approximation within more inner product. On the other hand, the discrete forms on second-order partial derivative exist different numerical performances in Table 1, which possess the similar conclusion between FPM and SPH<sup>[70]</sup>. The capacity of current hybrid particle approximation mainly depends on the computational fidelity of quantum procedure.

These numerical performances on multi-partitioned zones and ancilla qubits for QPE estimation are recorded in Table 2 and Fig.(11). It is obvious that the accuracy on QPE estimation depends on ancilla qubits. The small size computation of inner product by multi-partitioned zones is advantaged than that without partitioned procedure shown in Figs.(11a,11c). This multi-partitioned strategy can also improve the utilization efficiency on quantum register and satisfy the current stored limitation on NISQ device especially in 3-D particle dynamics.

$$F(x, y) = x^2 + y^2 \quad (65)$$

$$F(x, y) = \sin(10x) \cos(10y) \quad (66)$$

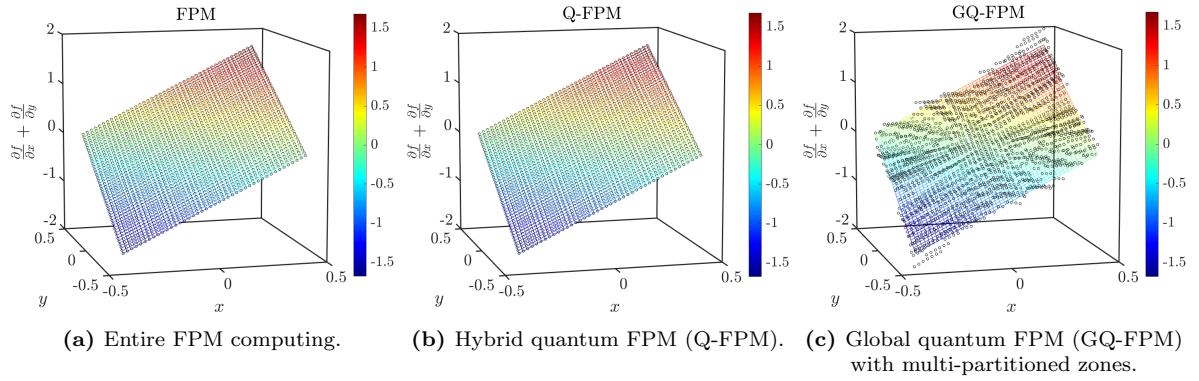


**Fig. 10** Numerical approximation on first-order partial derivative.

**Table 1** Relative  $L_2$  norm error evaluations on different computing modules.

Derivative	FPM	Q-FPM	GQ-FPM
First-order	$1.0917 \times 10^{-7}$	$2.7992 \times 10^{-4}$	$1.3934 \times 10^{-1}$
Second-order (Like-diff)	$9.7665 \times 10^{-6}$	$2.7984 \times 10^{-4}$	$1.6638 \times 10^{-0}$
Second-order (Nested sum)	$1.4013 \times 10^{-6}$	$5.6018 \times 10^{-4}$	$3.2616 \times 10^{-1}$

**Table 2** Relative  $L_2$  norm error evaluations on different ancilla qubits with multi-partitioned zones.

Derivative	No Partition	QPE 2	QPE 4	QPE 6	QPE 8
First-order	$2.9506 \times 10^{-1}$	$7.0863 \times 10^{-1}$	$1.3934 \times 10^{-1}$	$2.9278 \times 10^{-2}$	$7.1423 \times 10^{-3}$
Second-order (Like-diff)	$9.9891 \times 10^{-1}$	$3.5114 \times 10^{-0}$	$1.6638 \times 10^{-0}$	$4.4617 \times 10^{-1}$	$1.0890 \times 10^{-1}$
Second-order (Nested sum)	$7.3994 \times 10^{-1}$	$2.1146 \times 10^{-0}$	$3.2616 \times 10^{-1}$	$8.6567 \times 10^{-2}$	$1.9793 \times 10^{-2}$



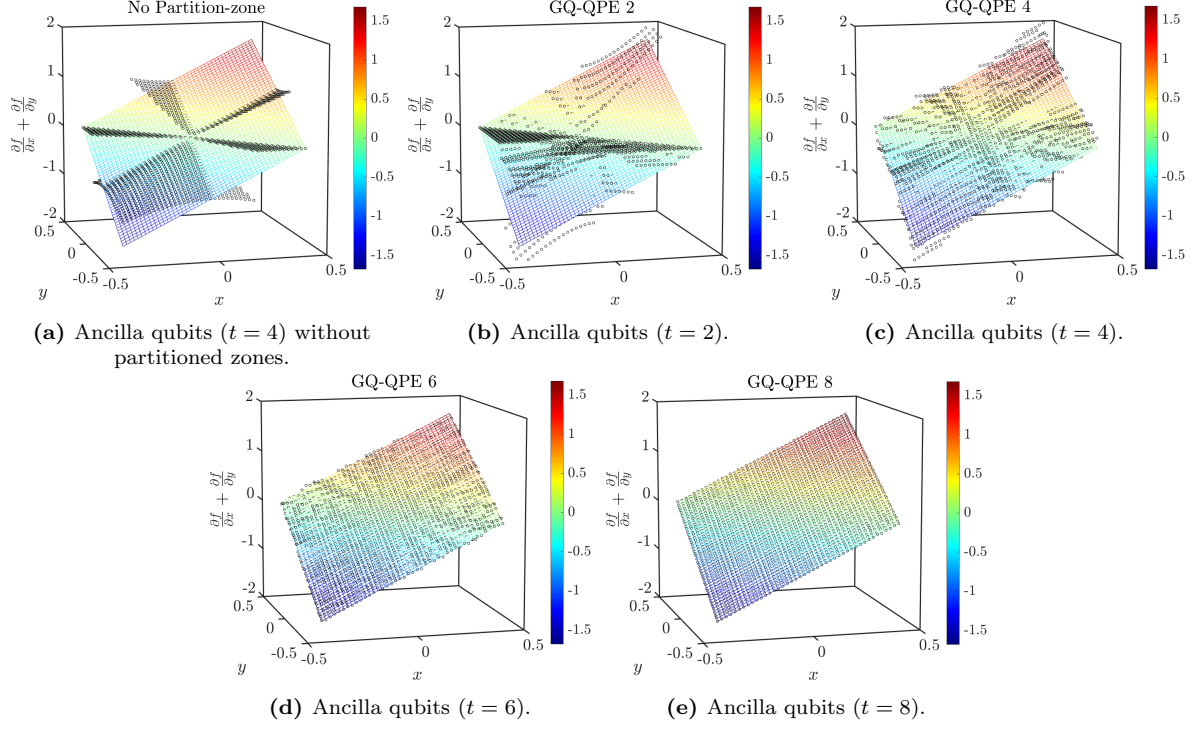


**Fig. 11** Numerical approximation (meshfree FPM) on different ancilla qubits with multi-partitioned zones.

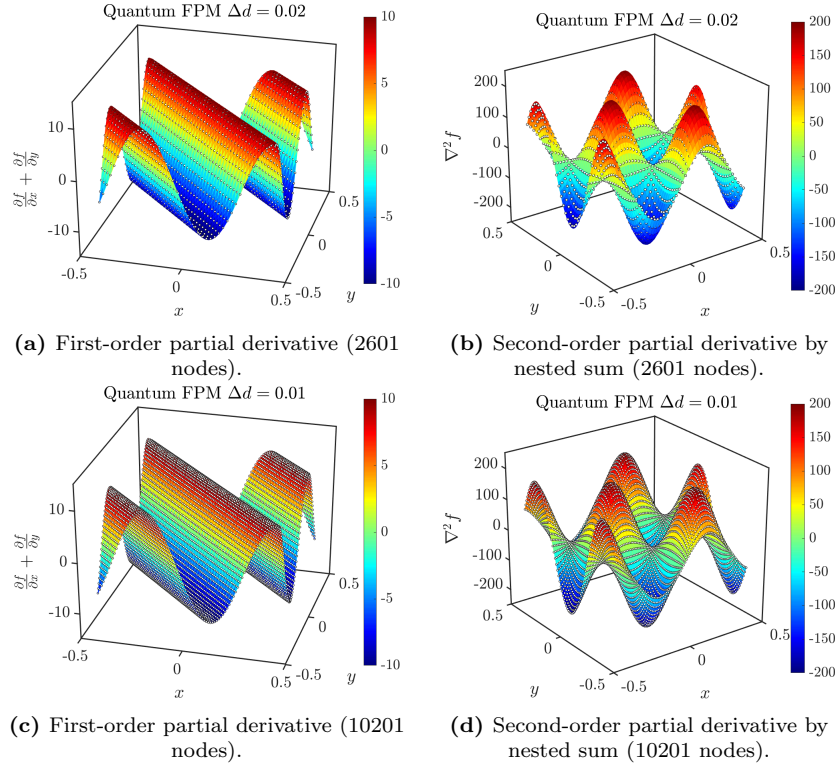


**Fig. 12** Global quantum FPM approximation using different particle interval.

Subsequently, considering more complicated variations on surface functions, it is validated based on the hybrid quantum computing of Eq.(66). As shown in Fig.(12), we adopted the aforementioned quantum FPM algorithm to capture the derivative changes of surface function using different particle interval  $\Delta d$ . Based on the complicated changes of second-order derivative, we captured the particle morphology in Figs.(13,14) by using different discrete forms to further investigate their numerical performances on hybrid



quantum procedures. Differently from conventional meshfree particle approximation, it is sensitive on the QPE estimation and the manifestation of denominator singularity  $1/r_{ij}^2$  in Eq.(30). It is further concluded that the small size of computation possesses the better quantum fidelity with multi-partitioned zones and the discrete form on repetitive nested sum has the advantaged accuracy originally from high-precision approximated capability of finite particle method. Some details of conventional numerical performance for different mathematical methods can be referenced to an extent<sup>[70]</sup>.

Additionally, the on-going time consumption and algorithmic convergence on present hybrid particle dynamics are also described detailedly in Table 3 and Fig.(15). It is observed that the present hybrid procedure has a stable convergent state reaching to error 0.5% when  $\Delta d = 5$  mm. The inclusion of additional auxiliary qubits in QPE also leads to exponentially growing computational time requirements as particle spacing refinement increases. It notes that the accuracy degradation in hybrid quantum FPM implementations, while unavoidable given current NISQ-era device constraints (gate fidelity, coherence times), represents a necessary trade-off for pioneering quantum-classical computational synergies. Its strategic importance persists as qubit scalability and error correction technologies maturely.

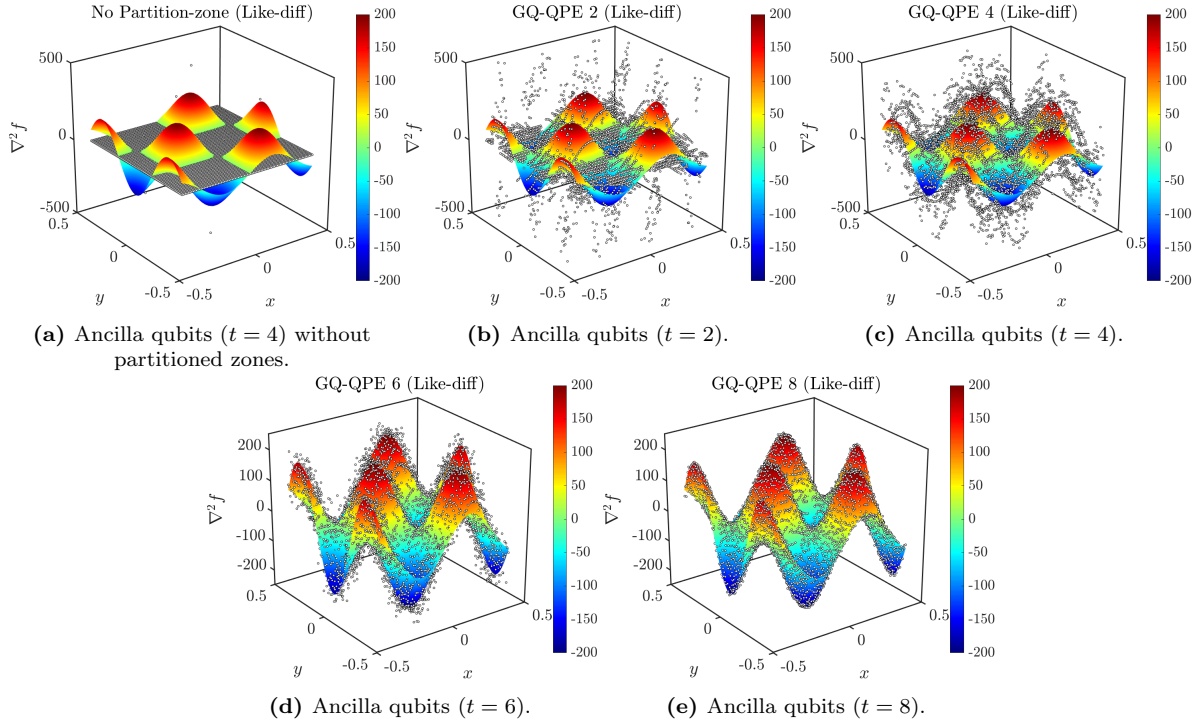


**Fig. 13** Second-order partial derivative on approximated like-difference form.

**Table 3** Time consuming on present validation procedures.

Interval $\Delta d$	Function	No Partition	QPE 2	QPE 4	QPE 6	QPE 8
0.02	(Fun1)	151.192 s	73.319 s	82.174 s	159.764 s	536.649 s
	(Fun2)	152.786 s	74.416 s	88.356 s	162.471 s	553.983 s
0.01	(Fun1)	680.269 s	345.125 s	410.021 s	726.124 s	2498.25 s
	(Fun2)	684.161 s	349.456 s	414.895 s	737.772 s	2531.63 s

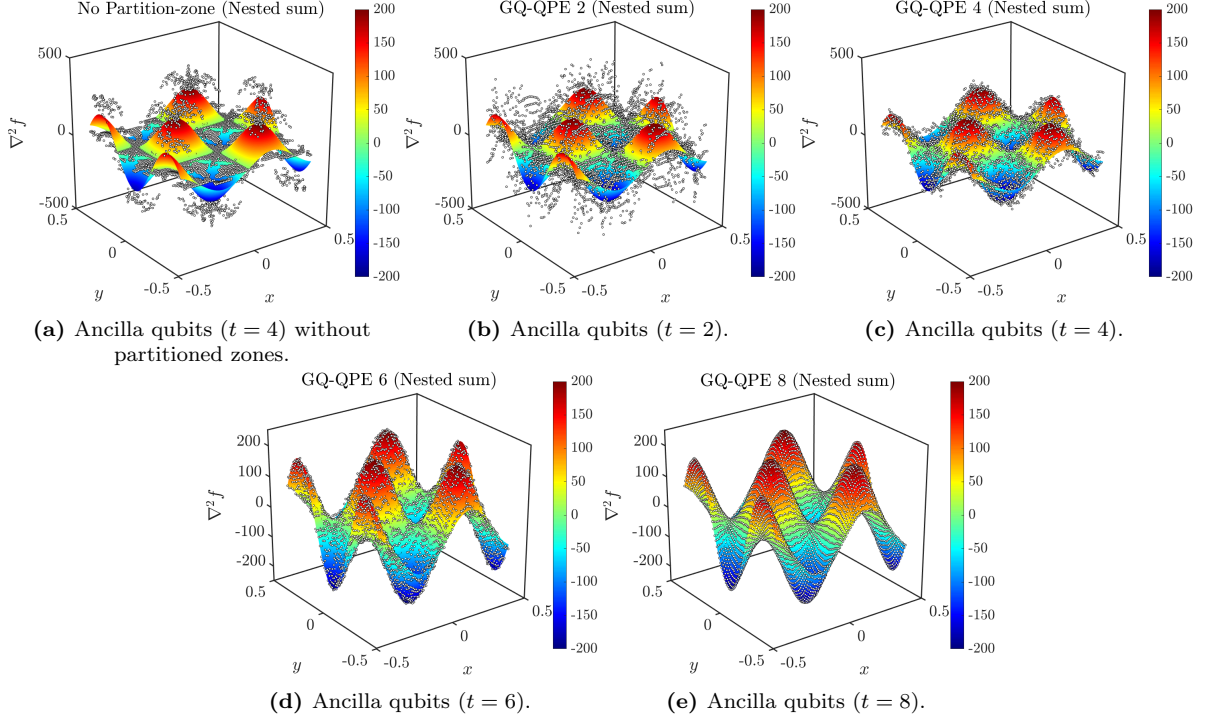


**Fig. 14** Second-order partial derivative on approximated nested sum form.

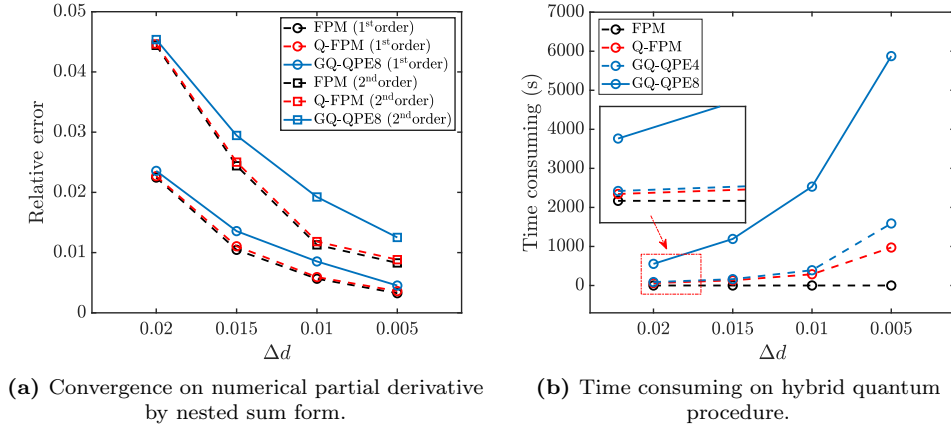


**Fig. 15** Numerical approximation with the refinement of particle spacing.

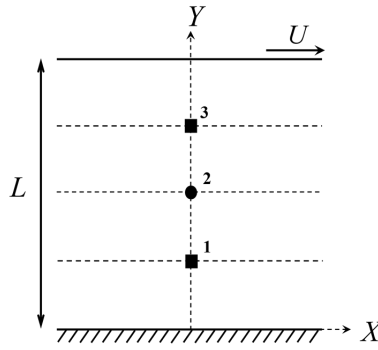
## Case 2: Dynamic viscoelastic Couette flow

This subsection presents a targeted verification of the proposed hybrid quantum FPM approach involving a time-dependent flow procedure. The unsteady Couette flow of Oldroyd-B viscoelastic fluids is validated. As shown in Fig.(16), the configuration consists of two infinite parallel plates and the bottom plate remains stationary while the top plate moves at a constant velocity  $U = 0.01$  m/s. A transient shear flow driven periodically by a shear stress parallel to the X-axis is simulated. Analytical solutions for this Oldroyd-B flow are available in the literature<sup>[46]</sup>. The characteristic velocity and length are set to  $U = 1$  m/s and  $L = 1$  m, respectively. The Reynolds number is defined as  $Re = \rho UL/\mu$ , the Weissenberg number as  $We = \lambda_1 U/L$ , and the ratio of viscoelasticity as  $\beta_0 = \mu_s/(\mu_s + \mu_p)$ . Simulations are conducted across various Reynolds and Weissenberg numbers. Velocity profiles are probed at three fixed locations within the flow domain, as indicated in Fig.(16). The smoothing kernel length is set to  $h = 1.4d_0$ , where  $d_0$  is the initial particle spacing, and the time step is  $\Delta t = 1 \times 10^{-4}$  s.

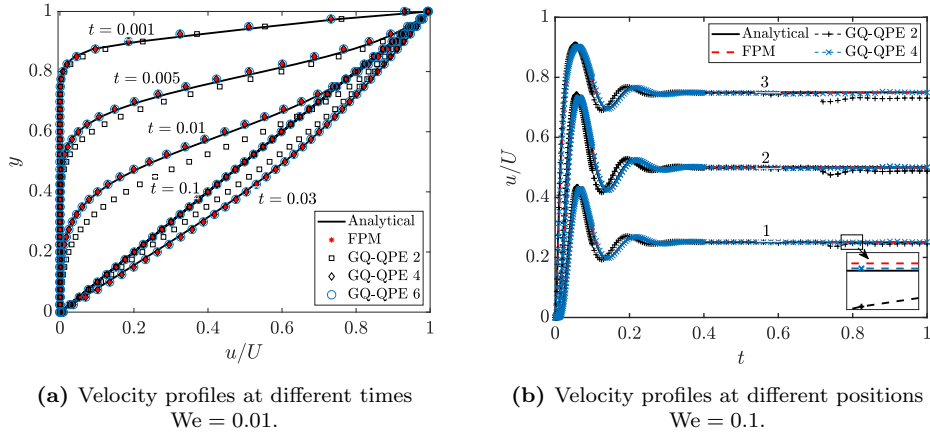
Figs.(17-18) give different physical descriptions and numerical comparisons among these numerical results and analytical solutions. The numerical phenomenon reveals a time-dependent increase in the velocities of bottom fluid, attributed to the viscoelastic stress effects shown in Fig.(17a). For the viscoelastic

fluid flow, particle velocity overshoot is observed, wherein fluid particles exhibit a transient peak velocity in Fig.(17b). Subsequently, the velocity fluctuations attenuate progressively until the system stabilizes into a linear particle motion. Fig.(18) presents the numerical results at varying spatial positions and Weissenberg numbers. Key findings indicate that both the particle velocity overshoot and fluctuations diminish with increasing Weissenberg numbers  $We$ , correlating with the weakening viscoelastic effects.

Based on the advantaged multi-partitioned quantum computing with the frame on computational FPM method, the long-time evolutional quantum inner product process with 4 or 6 ancillary qubits achieves the favorable computational accuracy comparable to classical FPM method, while demonstrating excellent agreements with exact solutions. In contrast, the computational procedure employing only 2 ancillary qubits exhibits inferior performance, yielding significantly less accurate results in quantum phase estimation (QPE) measurements. As a result, the current results of designed dynamic viscoelastic Couette flow obviously confirm the validity of hybrid quantum-classical computational approach, while demonstrating the potential for implementing quantum computing in long-term evolution simulations of particle-laden fluid dynamics. This comprehensive methodology enables more extensive and in-depth integrated computations.

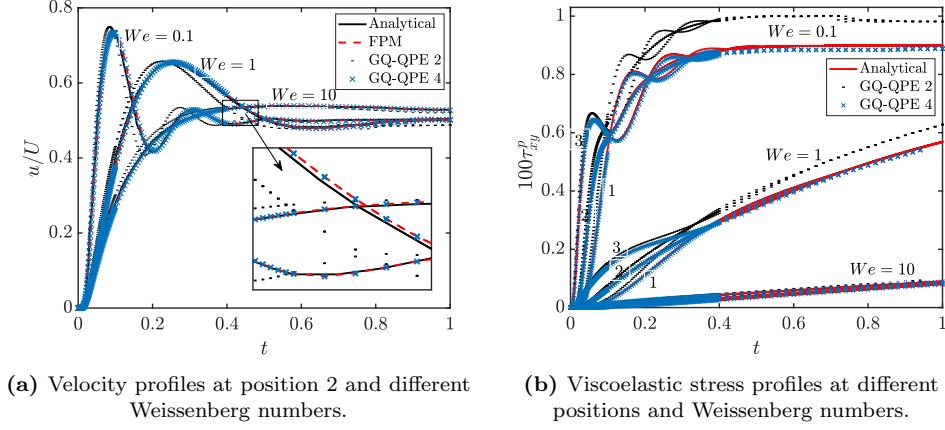


**Fig. 16** Physical model of Couette planar flow.



**Fig. 17** Velocity overshoot of viscoelastic Couette flow. ( $Re = 0.05$ ,  $\beta_0 = 0.1$ )

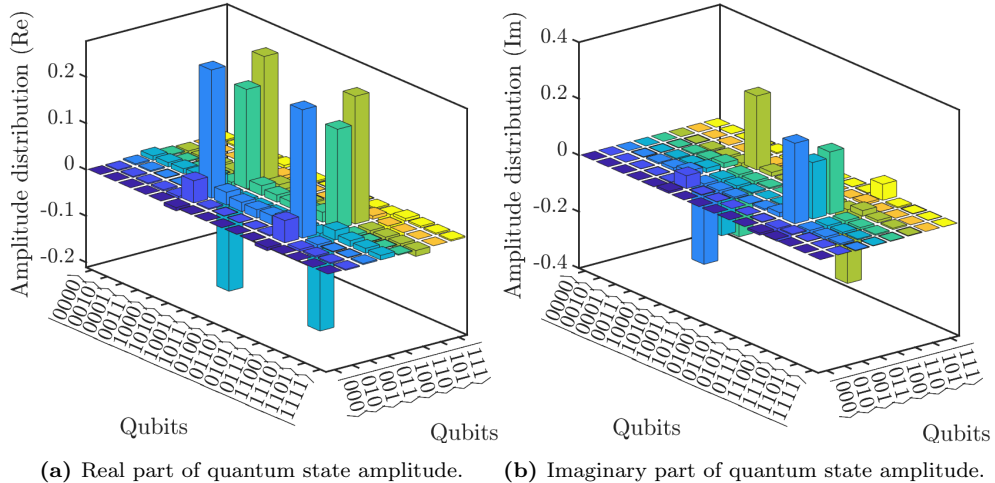
Moreover, the computational accuracy of current hybrid quantum inner product process is critically dependent on the number of ancillary qubits in QPE shown in Fig.(7), particularly when accounting for quantum noise in noisy intermediate-scale quantum (NISQ) devices. Under such conditions, quantum measurement outcomes and state collapse behaviors exhibit significant variations. As emerging quantum-enhanced techniques, including variational quantum algorithms (VQAs)<sup>[39]</sup> and quantum machine learning approaches, it demonstrated the improved capability for evaluating numerical solutions of quantum inner product and achieving fidelity. While the QPE-based inner product methodology remains fundamentally robust when considering the computational continuity and integrality requirements in fluid dynamics simulations<sup>[5, 67]</sup>.



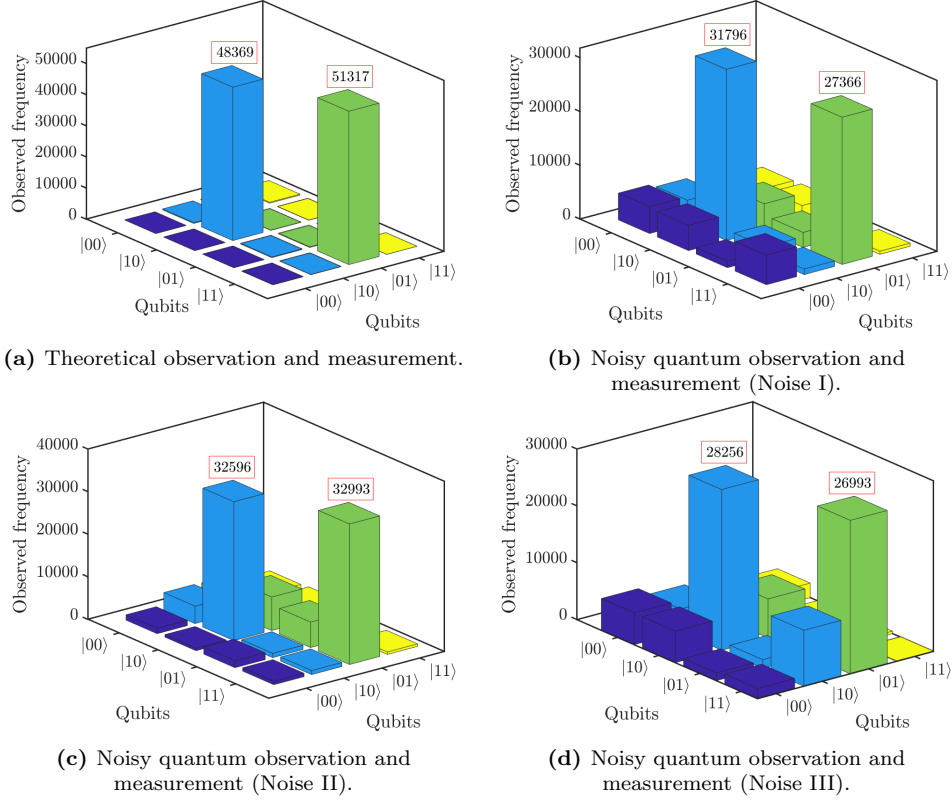
**Fig. 18** Numerical results of viscoelastic Couette flow in hybrid quantum FPM. ( $Re = 0.1$ ,  $\beta_0 = 0.1$ )

Fig.(19) illustrates the composite Hilbert space formed by ancillary and measurement qubits in the present hybrid quantum FPM procedure. The observed probability amplitude distribution within this state space governs the measurement-induced wave function and collapse statistics, where the squared modulus of these amplitudes  $|\langle u|w\rangle|^2$  determines the projective measurement probabilities according to the Born rule. In this study, to rigorously evaluate the hybrid numerical performance, we conducted 100,000 effective experimental trials of noisy QPE computing, as demonstrated in Fig.(20). The noisy quantum incorporated the variational decoherence noise models and distinct energy relaxation rates during the measurement processes. This approach ensures computational reliability and facilitates practical hybrid computation implementation on current NISQ devices. Despite inherent noise interference, the robust QPE protocol successfully captures accurate computational results through statistically significant sampling (100,000 quantum measurements), demonstrating the favorable hybrid computation performance.

Finally, Table 4 summarizes the operational statistics of 735 FPM particles encoded in multi-partitioned quantum registers. The number of ancillary qubits emerges as the dominant factor governing total computation time, particularly for large-scale models requiring multiple iteration steps. Under these conditions, the temporal cost significantly exceeds classical computational scales (by 2 – 3 orders of magnitude), reflecting fundamental limitations in current quantum phase estimation implementations and quantum device architectures generally. Notably, quantum computing demonstrates the inherent advantages for small-scale, single-step computations, achieving latencies as low as  $10^{-7}$  s (seeing Table 4). However, the analysis reveals substantial developmental requirements for complex, large-scale dynamical computations, particularly regarding temporal efficiency and precision maintenance in noisy environments. As a result, the present hybrid quantum-classical approaches remain essential for transitional-stage implementations. We anticipate that the continued development of quantum hardware will further enhance the reliability and robustness of these quantum computational outcomes.



**Fig. 19** Quantum state amplitudes in high-dimensional Hilbert space.



**Fig. 20** Quantum measurements and state collapse through 100,000 single-molecule observations.

**Table 4** Operational statistics of 735 FPM particles multi-partially encoded in quantum registers.

QPE	Total steps on quantum register	Observed frequency	Total time	Time at per particle	Time at per particle and step	Time at per particle step and measurement
2	20,002	100,000	241,273 s	328.26 s	0.01641 s	$1.641 \times 10^{-7}$ s
4	20,002	100,000	306,740 s	417.33 s	0.02086 s	$2.086 \times 10^{-7}$ s

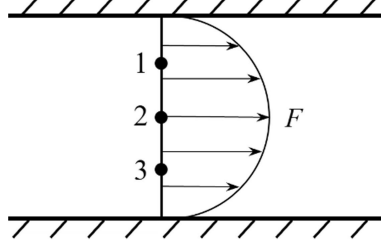
### Case 3: Dynamic viscoelastic Poiseuille flow with HWN discussion

In this subsection, numerical analysis on high Weissenberg viscoelastic fluid flow is further investigated based on present hybrid quantum computing procedure. Notably, given the inherent limitations of current quantum simulation algorithms and the non-trivial computational overhead of hybrid quantum-particle operations quantified in Table 4, this work employs viscoelastic Poiseuille flow as a benchmark system to rigorously evaluate the HWN behaviors and improved meshfree numerical performance on accuracy and convergence. Through this paradigm, we demonstrated both methodological novelty and computational potential of the developed FPM framework and the quantum-hybridized implementation.

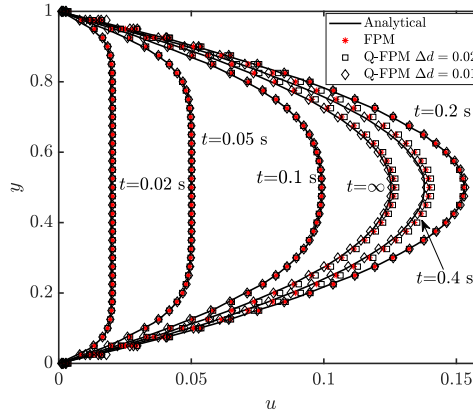
The schematic representation of present Poiseuille flow system is depicted in Fig.(21), specifying the unit-length spacing between two infinite parallel plates maintained in a stationary state. The computational setup employs periodic boundary conditions in horizontal direction, where a constant external force  $F = 1$  N applied in the positive x-direction drives the viscoelastic fluid flows through the resultant shear stress until achieving balanced laminar motion. Three equidistant sampling probes are strategically placed to quantify the evolution on physical field variables. The dimensionless parameters are characterized by Reynolds number  $Re = \rho UL/\mu$ , Weissenberg number  $We = \lambda_1 U/L$ , and ratio of viscoelasticity  $\beta = \mu_s/(\mu_s + \mu_p)$ . The characteristic velocity is  $U = 0.1$  m/s, the characteristic length is  $L = 1$  m and  $\Delta d$  denotes the initial spatial distance.

Fig.(22) captured the evolutionary velocity with analytical solutions<sup>[72]</sup> at different time, which can demonstrate the computational accuracy of present numerical scheme and show excellent agreements on quantum FPM. During the transient flow development, the characteristic velocity overshoot phenomenon caused by viscoelastic effects is clearly captured before reaching steady-state pipe flow. Comparative velocity profiles under steady-state conditions reveal the relative errors of 1.37% (FPM), 1.91% (present

Q-FPM with  $\Delta d = 0.02$ ) and 0.50% (present Q-FPM with  $\Delta d = 0.01$ ), respectively. In Fig.(23), the viscoelastic stress components are also computed across varying initial particle spacings, demonstrating satisfactory convergence behavior. With progressive particle refinements, numerical discrepancies near boundaries systematically diminish, asymptotically approaching the analytical solution<sup>[72]</sup>. Therefore, the effectiveness of current hybrid quantum-particle dynamics approach can be demonstrated through the quantum-classical coupling accuracy and convergence.



**Fig. 21** Sketch of viscoelastic Poiseuille flow.



**Fig. 22** Profile on measured velocity by present quantum FPM procedure.

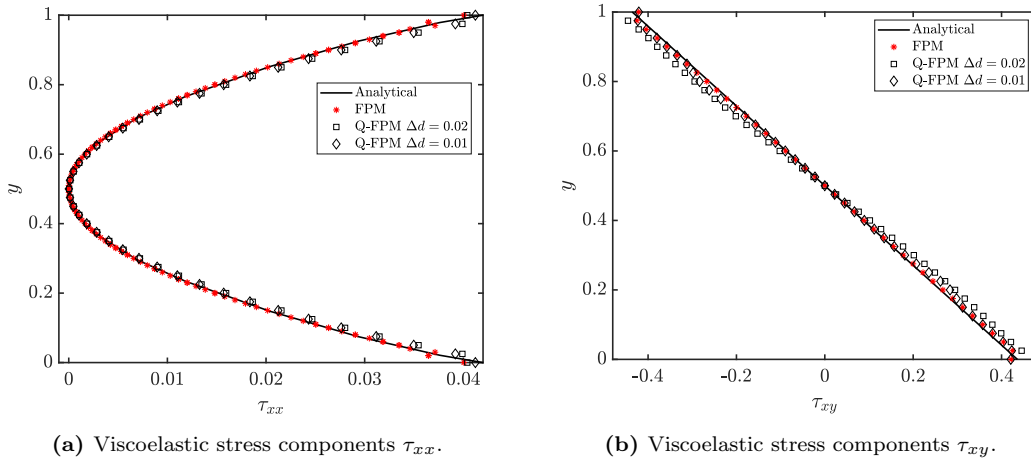


**Fig. 23** Profile on measured viscoelastic stress components at steady flow state.

Subsequently, based on the developed quantum FPM approach and Log conformation evolution, it is further focus on the high Weissenberg viscoelastic fluid flow and classical formulations of Oldroyd-B and UCM constitutive models. As shown in Fig.(24), the velocity evolution and dominant shear stress development in Poiseuille flow are computed across varying ratio of viscoelasticity  $\beta = \mu_s/(\mu_s + \mu_p)$  under specified Reynolds number and relatively low Weissenberg number. It is observed that with increasing ratios  $\beta$  (enhanced viscous dominance), the flow characteristics asymptotically approach Newtonian fluid



behaviors. The spatial positions of fluid probes 1 and 2 are explicitly defined in Fig.(21). Notably, with increasing elastic contributions, the flow procedure exhibits progressively pronounced velocity overshoot phenomena accompanied with fluctuating velocity distributions. When the ratio parameter  $\beta = 0$ , the fluid model is transformed to the constitutive UCM model, which possibly exists inherent numerical instabilities and singularities in peak velocity variations. To address these computational challenges, the artificial viscosity method in Eq.(44) is typically employed similarly as the elasto-viscous stress splitting (EVSS) technique in finite element analysis<sup>[57,73]</sup>, where controlled introduction of numerical dissipation stabilizes the numerical solutions while maintaining essential physical fidelity.

The absence of viscous terms transforms the momentum equation from a parabolic form (as in Newtonian or Oldroyd-B fluids) to a hyperbolic partial differential equation (as in purely elastic UCM fluids). This loss of explicit dissipation often results in numerical instability or divergence of the solution. Stabilization approaches such as BSD, EVSS, and AVSS, mitigate these issues by reintroducing elliptic operators into the momentum equation, thereby effectively restoring its parabolic character in a manner analogous to artificial viscosity. For instance, the techniques like EVSS augment viscous dissipation to preserve numerical stability. Nevertheless, as the Weissenberg number rising, these instabilities become more pronounced until a critical threshold is reached, the value of which depends on both the constitutive model and the numerical scheme adopted.

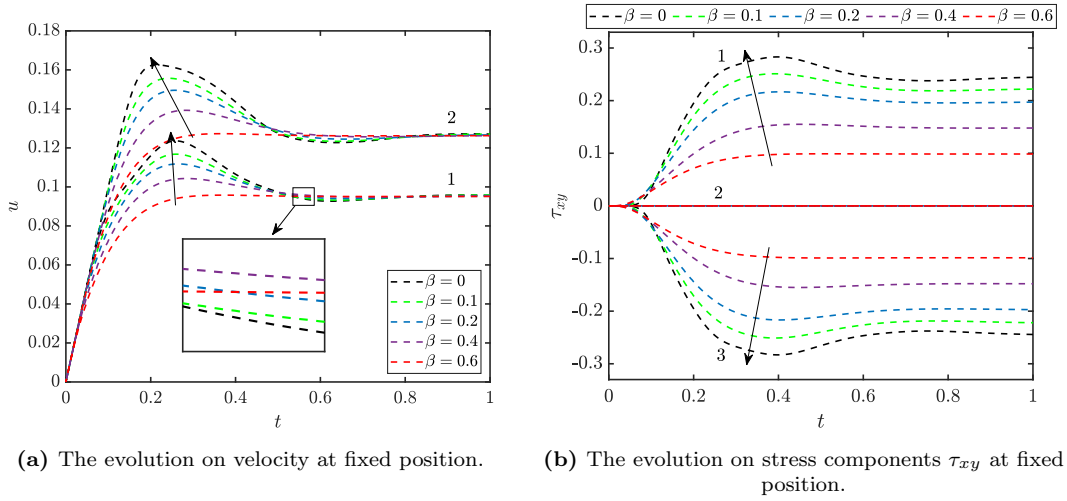


**Fig. 24** Numerical evolution on present hybrid quantum FPM with the ranging of ratio of viscoelasticity  $\beta$ . ( $Re = 0.1$ ,  $We = 0.01$ )

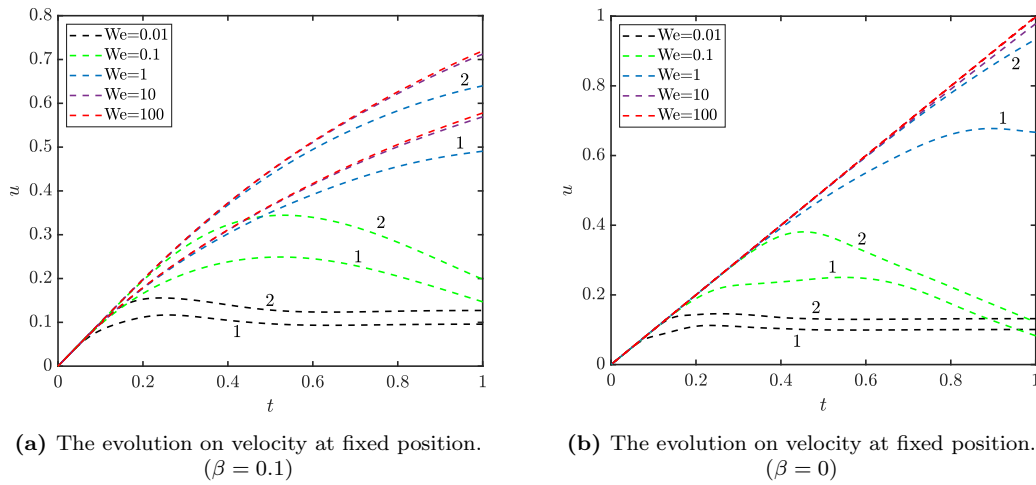


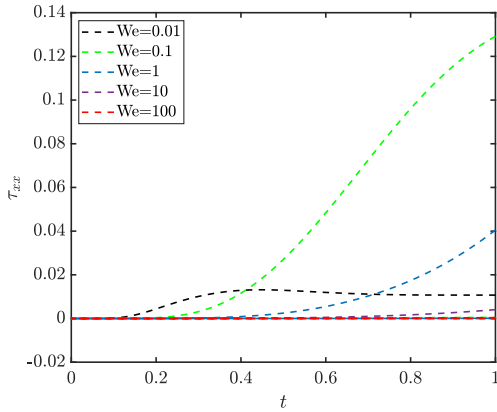
**Fig. 25** Numerical evolution on present hybrid quantum FPM with the increasing of Weissenberg number  $We$ . ( $Re = 0.1$ )

Further, we investigated the viscoelastic flow behaviors with the increasing of Weissenberg number based on the present Oldroyd-B and typical UCM constitutive models. Through the entire quantum-

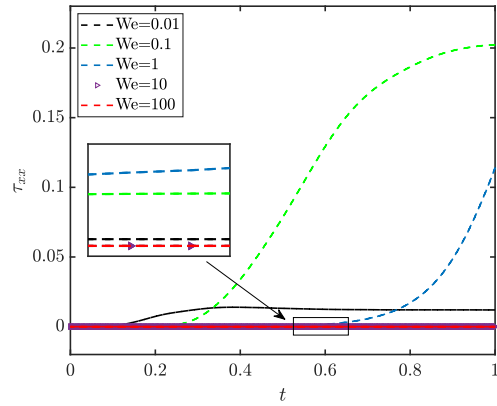


hybrid computing and HWN-resolving Log conformation approach, numerical instability can be effectively suppressed combining with additional artificial viscosity. As illustrated in Fig.(25), the velocity evolution of viscoelastic Poiseuille flow computed by the current numerical framework is presented, with particular emphasis on the progression at locations of Probe 1 and Probe 2. It can be observed that with the increasing of Weissenberg number, the velocity profile exhibits a more linearized trend. The purely elastic upper convected Maxwell (UCM) model demonstrates a pronounced tendency for sharp velocity gradients at extreme points, a behavior consistent with the manifestations detailed in Fig.(24). Additionally, as the Weissenberg number increasing, the discrepancy of velocity between Positions 1 and 2 diminishes significantly. At  $We = 100$ , the velocity variations across different heights become nearly identical, indicating that the interlayer shear stress inducing nonlinear velocity changes, converges to the same distribution regardless of vertical positions.

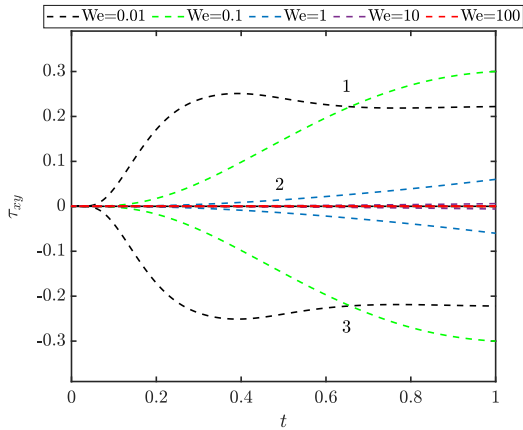
The specific manifestations underlying this trend can be observed from the evolution of elastic stress components in Fig.(26). In conjunction with the time-dependent viscoelastic constitutive equations, explicit form of Eq.(42) and logarithmic form of Eq.(60), the qualitative analysis confirms that as the relaxation time  $\lambda_1$  increasing in corresponding Weissenberg number, the temporal variations of elastic stress are primarily governed by their velocity gradients and existing stress fields. The viscous shear stress term of constitutive model serves as the main driver for interlayer flow. A gradual reduction in this viscous component leads to a significant decrease in interlayer shear, thereby resulting in the velocity trends described in above figures. These mechanistic insights are corroborated by numerical changes in the elastic stress components depicted in Figs.(26b, 26d). The results also demonstrate that introducing artificial viscosity effectively suppresses numerical instabilities as the rationale underpinning techniques such as aforementioned EVSS approach, which explicitly decouples and stabilizes the numerical discretization on Navier Stokes equations.



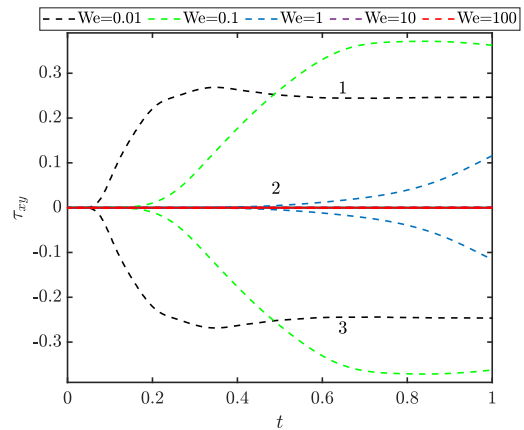
(a) The evolution on stress components  $\tau_{xx}$  at fixed position. ( $\beta = 0.1$ )



(b) The evolution on stress components  $\tau_{xx}$  at fixed position. ( $\beta = 0$ )



(c) The evolution on stress components  $\tau_{xy}$  at fixed position. ( $\beta = 0.1$ )



(d) The evolution on stress components  $\tau_{xy}$  at fixed position. ( $\beta = 0$ )

**Fig. 26** Numerical evolution on present hybrid quantum FPM with the increasing of Weissenberg number  $We$ . ( $Re = 0.1$ )

Finally, we extracted the velocity profiles on the pipe flow at time  $t = 1$  for Weissenberg numbers ranging sequentially from 0.01 to 100, as shown in Fig.(27). Consistent with the preceding analysis, at  $We = 10, 100$ , the viscous shear contribution becomes nearly negligible. The viscoelastic flow is predominantly driven by purely elastic stresses and the external force  $F$ , exhibiting a steady linear increase and distinct wall slip phenomena. This behavior aligns with the interfacial dynamics typical of highly elastic, purely elastic fluids under shear flows. Meanwhile, these advances provide critical insights for transitioning quantum-enhanced non-Newtonian fluid simulations toward practical engineering applications.

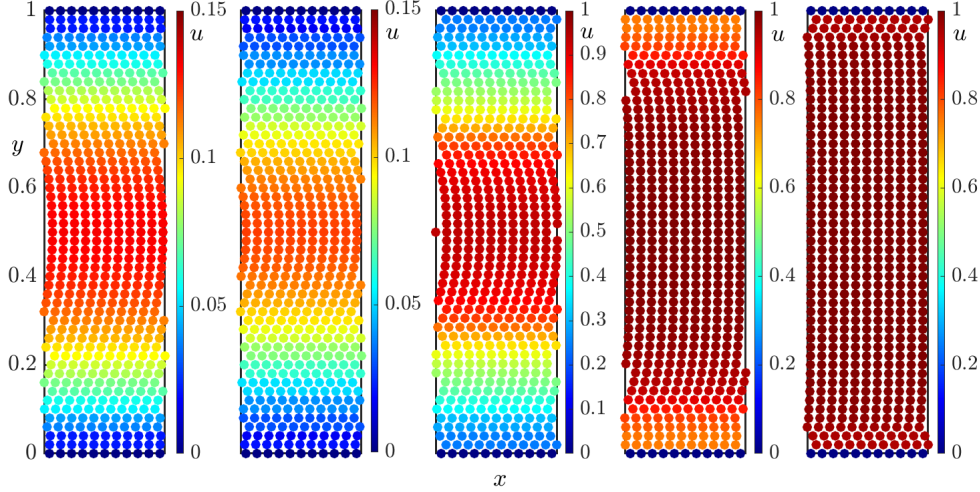


**Fig. 27** Profile on calculated velocities by present hybrid quantum computing, from left to right:  $We = 0.01, 0.1, 1, 10, 100$ . ( $Re = 0.1, \beta = 0$ )

## 6 Concluding remarks

In this study, we built a hybrid quantum framework for fluid flow, integrating multi-partitioned quantum zones with meshfree finite particle method. Through a purposefully designed sequence of numerical experiments, progressing from fundamental to complicated scenarios, the proposed methodology was thoroughly validated and analyzed. The results demonstrate that integrating quantum computing to hybridize conventional linear combinations in common computational particle dynamics serves as an effective high performance computing strategy. Furthermore, by extending the numerical investigation into viscoelastic, highly elastic, and purely elastic fluids under high Weissenberg number conditions, the applicability of quantum-hybrid algorithm is significantly broadened.

As represented by smoothed particle hydrodynamics (SPH), material point method (MPM), and current finite particle method (FPM) in meshfree computational particle dynamics, these numerical techniques such as corrected kernels for linear combinations and approximated difference operators for physical quantity smoothing can be implemented by adopting quantum bits to construct quantum states. Quantum processors' natural parallelism might enable the real-time modeling of massive particle systems, something that remains computationally prohibitive on traditional HPC architectures. Therefore, this approach establishes a foundation for the development of quantum-hybrid computing. Considering the limitations of current quantum devices (particularly in qubit counts) and associated computational costs, the multi-partitioned zones proposed in this study help to avoid prohibitive computational time in more complicated fluid simulations.

Similarly, while the established quantum algorithms such as the swap test for inner product and quantum phase estimation providing accurate inner product results, along with emerging variational quantum algorithms, this study still adopts the classical swap test and multi-ancilla QPE process for integration into the simulations. This decision is resulted from the current readiness of these methods for physics-based simulations and high performance quantum processing unit (QPU) computations, and it represents an original attempt at such integration within the meshfree finite particle framework firstly.

It is undeniable that several limitations remain, including quantum hardware constraints, fidelity issues, and computational overhead in three-dimensional simulations. This work should therefore be regarded as a preliminary effort and foundational study in quantum-classical hybrid computing. In alignment with the perspective<sup>[34, 40–42]</sup>, quantum computers are unlikely to entirely replace classical sys-

tems but rather function through hybrid mechanisms. This research expands the scope of hybrid high performance computing that integrates quantum co-processors and QPU architectures with traditional particle-based methods. It contributes a meaningful basis for future scientific and technological advances in quantum hardware and computational fluid dynamics, and will continue to evolve with ongoing developments.

**Acknowledgements** This work has been partially supported by the National Natural Science Foundation of China [Grant Nos. 12032002 and U22A20256] and the Sino-German Mobility Programme [No. M-0210].

## References

- [1] F. Tennie, S. Laizet, S. Lloyd, L. Magri, Quantum computing for nonlinear differential equations and turbulence, *Nature Reviews Physics* (2025) 1–11.
- [2] N. Defenu, A. Lerose, S. Pappalardi, Out-of-equilibrium dynamics of quantum many-body systems with long-range interactions, *Physics Reports* 1074 (2024) 1–92.
- [3] R. Au-Yeung, B. Camino, O. Rathore, V. Kendon, Quantum algorithms for scientific computing, *Reports on Progress in Physics* 87 (11) (2024) 116001.
- [4] S. J. Thomson, J. Eisert, Unravelling quantum dynamics using flow equations, *Nature Physics* 20 (9) (2024) 1401–1406.
- [5] Z. Y. Chen, T. Y. Ma, C. C. Ye, L. Xu, W. Bai, L. Zhou, et al., Enabling large-scale and high-precision fluid simulations on near-term quantum computers, *Computer Methods in Applied Mechanics and Engineering* 432 (2024) 117428.
- [6] C. C. Ye, N. B. An, T. Y. Ma, M. H. Dou, W. Bai, D. J. Sun, Z. Y. Chen, G. P. Guo, A hybrid quantum-classical framework for computational fluid dynamics, *Physics of Fluids* 36 (12) (2024) 127111.
- [7] T. Muther, A. K. Dahaghi, F. I. Syed, V. V. Pham, Physical laws meet machine intelligence: current developments and future directions, *Artificial Intelligence Review* 56 (7) (2022) 6947–7013.
- [8] E. G. Rieffel, A. A. Asanjan, M. S. Alam, N. Anand, D. E. Bernal Neira, S. Block, L. T. Brady, S. Cotton, Z. Gonzalez Izquierdo, et al., Assessing and advancing the potential of quantum computing: A nasa case study, *Future Generation Computer Systems* 160 (2024) 598–618.
- [9] S. S. Bharadwaj, K. R. Sreenivasan, Hybrid quantum algorithms for flow problems, *Proceedings of the National Academy of Sciences* 120 (49) (2023) 2311014120.
- [10] M. Lubasch, J. Joo, P. Moinier, M. Kiffner, D. Jaksch, Variational quantum algorithms for nonlinear problems, *Physical Review A* 101 (01 2020).
- [11] O. Kyriienko, A. Paine, V. Elfving, Solving nonlinear differential equations with differentiable quantum circuits, *Physical Review A* 103 (05 2021).
- [12] B. N. Todorova, R. Steijl, Quantum algorithm for the collisionless boltzmann equation, *Journal of Computational Physics* 409 (2020) 109347.
- [13] Y. Sato, R. Kondo, S. Koide, H. Takamatsu, N. Imoto, Variational quantum algorithm based on the minimum potential energy for solving the poisson equation, *Physical Review A* 104 (2021) 052409.
- [14] B. Jaderberg, A. A. Gentile, A. Ghosh, V. E. Elfving, C. Jones, D. Vodola, J. Manobianco, H. Weiss, Potential of quantum scientific machine learning applied to weather modelling, *Physical Review A* (5) (2024) 110.
- [15] T. Belytschko, Y. Krongauz, D. Organ, M. Fleming, P. Krysl, Meshless methods: An overview and recent developments, *Computer Methods in Applied Mechanics and Engineering* 139 (1) (1996) 3–47.
- [16] G. R. Liu, Y. T. Gu, A meshfree method: meshfree weak–strong (mws) form method, for 2-d solids, *Computational Mechanics* 33 (2003) 2–14.
- [17] G. R. Liu, An overview on meshfree methods: for computational solid mechanics, *International Journal of Computational Methods* 13 (05) (2016) 1630001.
- [18] V. P. Nguyen, T. Rabczuk, S. Bordas, M. Duflo, Meshless methods: A review and computer implementation aspects, *Mathematics and Computers in Simulation* 79 (3) (2008) 763–813.
- [19] R. A. Gingold, J. J. Monaghan, Smoothed particle hydrodynamics: theory and application to non-spherical stars, *Monthly Notices of the Royal Astronomical Society* 181 (3) (1977) 375–389.
- [20] J. J. Monaghan, Smoothed particle hydrodynamics, *Annual Review of Astronomy and Astrophysics* 30 (1992) 543–574.
- [21] T. Belytschko, Y. Y. Lu, L. Gu, Element-free galerkin methods, *International Journal for Numerical Methods in Engineering* 37 (2) (1994) 229–256.
- [22] J. W. Swegle, D. L. Hicks, S. W. Attaway, Smoothed particle hydrodynamics stability analysis, *Journal of Computational Physics* 116 (1) (1995) 123–134.
- [23] M. B. Liu, G. R. Liu, K. Y. Lam, Constructing smoothing functions in smoothed particle hydrodynamics with applications, *Journal of Computational and Applied Mathematics* 155 (2) (2003) 263–284.
- [24] M. S. Shadloo, G. Oger, D. Le Touzé, Smoothed particle hydrodynamics method for fluid flows, towards industrial applications: Motivations, current state, and challenges, *Computers & Fluids* 136 (2016) 11–34.
- [25] Y. Y. Lu, T. Belytschko, L. Gu, A new implementation of the element free galerkin method, *Computer Methods in Applied Mechanics and Engineering* 113 (3-4) (1994) 397–414.
- [26] B. Nayroles, G. Touzot, P. Villon, Generalizing the finite element method: diffuse approximation and diffuse elements, *Computational Mechanics* 10 (5) (1992) 307–318.

- [27] E. Kansa, Multiquadrics—a scattered data approximation scheme with applications to computational fluid-dynamics—i surface approximations and partial derivative estimates, *Computers and Mathematics with Applications* 19 (8) (1990) 127–145.
- [28] G. E. Fasshauer, Solving differential equations with radial basis functions: multilevel methods and smoothing, *Advances in Computational Mathematics* 11 (2) (1999) 139–159.
- [29] G. R. Liu, M. B. Liu, *Smoothed particle hydrodynamics: a meshfree particle method*, World scientific, 2003.
- [30] X. D. Wang, W. K. Liu, Extended immersed boundary method using fem and rkpm, *Computer Methods in Applied Mechanics and Engineering* 193 (12–14) (2004) 1305–1321.
- [31] S. N. Atluri, T. Zhu, A new meshless local petrov-galerkin (mlpg) approach in computational mechanics, *Computational Mechanics* 22 (2) (1998) 117–127.
- [32] N. Aluru, A point collocation method based on reproducing kernel approximations, *International Journal for Numerical Methods in Engineering* 47 (6) (2000) 1083–1121.
- [33] S. Garg, M. Pant, Meshfree methods: a comprehensive review of applications, *International Journal of Computational Methods* 15 (04) (2018) 1830001.
- [34] K. Bharti, A. Cervera-Lierta, T. H. Kyaw, T. Haug, S. Alperin-Lea, A. Anand, M. Degroote, H. Heimonen, J. S. Kottmann, et al., Noisy intermediate-scale quantum algorithms, *Reviews of Modern Physics* 94 (2022) 015004.
- [35] A. Y. Kitaev, Quantum measurements and the abelian stabilizer problem (1995). [arXiv:quant-ph/9511026](https://arxiv.org/abs/quant-ph/9511026).
- [36] L. K. Grover, A fast quantum mechanical algorithm for database search, *Physical Review Letters* 79 (1997).
- [37] N. Shenvi, J. Kempe, K. B. Whaley, Quantum random-walk search algorithm, *Physical Review A* 67 (2003) 052307.
- [38] A. W. Harrow, A. Hassidim, S. Lloyd, Quantum algorithm for linear systems of equations, *Physical Review Letters* 103 (2009) 150502.
- [39] M. Cerezo, A. Arrasmith, R. Babbush, S. C. Benjamin, S. Endo, K. Fujii, J. R. McClean, K. Mitarai, X. Yuan, L. Cincio, P. J. Coles, Variational quantum algorithms, *Nature Reviews Physics* 3 (2021) 625–644.
- [40] L. S. Madsen, F. Laudenbach, M. F. Askarani, F. Rortais, T. Vincent, J. F. F. Bulmer, F. M. Miatto, L. Neuhaus, L. G. Helt, M. J. Collins, A. E. Lita, T. Gerrits, S. W. Nam, V. D. Vaidya, M. Menotti, I. Dhand, Z. Vernon, N. Quesada, J. Lavoie, Quantum computational advantage with a programmable photonic processor, *Nature* 606 (7912) (2022) 75–81.
- [41] N. Mitsuda, T. Ichimura, K. Nakaji, Y. Suzuki, T. Tanaka, R. Raymond, H. Tezuka, T. Onodera, N. Yamamoto, Approximate complex amplitude encoding algorithm and its application to data classification problems, *Physical Review A* 109 (2024) 052423.
- [42] K. M. Barnes, A. Buyskikh, N. Y. Chen, G. Gallardo, M. Ghibaudi, M. J. A. Ruszala, D. S. Underwood, A. Agarwal, D. Lall, I. Rungger, N. Schoinas, Optimising the quantum/classical interface for efficiency and portability with a multi-level hardware abstraction layer for quantum computers, *EPJ Quantum Technology* 10 (2023) 36.
- [43] Z. L. Zhang, K. Walayat, C. Huang, J. Z. Chang, M. B. Liu, A finite particle method with particle shifting technique for modeling particulate flows with thermal convection, *International Journal of Heat and Mass Transfer* 128 (2019) 1245–1262.
- [44] Z. L. Zhang, M. B. Liu, A decoupled finite particle method for modeling incompressible flows with free surfaces, *Applied Mathematical Modelling* 60 (AUG.) (2018) 606–633.
- [45] Y. D. Li, Y. Li, P. Joli, H. J. Chen, Z. Q. Feng, Extension of finite particle method simulating thermal-viscoelastic flow and fluid–rigid body interaction process in weakly compressible smoothed particle hydrodynamics scheme, *Physics of Fluids* 36 (4) (2024) 043307.
- [46] Y. D. Li, Y. Li, Z. Q. Feng, A coupled particle model with particle shifting technology for simulating transient viscoelastic fluid flow with free surface, *Journal of Computational Physics* 488 (2023) 112213.
- [47] M. B. Liu, W. P. Xie, G. R. Liu, Modeling incompressible flows using a finite particle method, *Applied Mathematical Modelling* 29 (12) (2005) 1252–1270.
- [48] M. B. Liu, G. R. Liu, Smoothed particle hydrodynamics (sph): an overview and recent developments, *Archives of Computational Methods in Engineering* 17 (1) (2010) 25–76.
- [49] T. Ye, D. Y. Pan, C. Huang, M. B. Liu, Smoothed particle hydrodynamics (sph) for complex fluid flows: Recent developments in methodology and applications, *Physics of Fluids* 31 (1) (2019) 011301.
- [50] F. Xu, J. Y. Wang, Y. Yang, L. Wang, Z. Dai, R. Q. Han, On methodology and application of smoothed particle hydrodynamics in fluid, solid and biomechanics, *Acta Mechanica Sinica* 39 (2) (2023) 1–36.
- [51] Y. D. Li, Y. Li, Z. Q. Feng, Extension of decoupled finite particle method to simulate non-isothermal free surface flow, *International Journal of Multiphase Flow* 167 (2023) 104532.
- [52] J. Benito, F. Ureña, L. Gavete, Influence of several factors in the generalized finite difference method, *Applied Mathematical Modelling* 25 (12) (2001) 1039–1053.
- [53] Y. D. Li, Z. J. Fu, Z. C. Tang, Generalized finite difference method for bending and modal analysis of functionally graded carbon nanotube-reinforced composite plates, *Chinese Journal of Theoretical and Applied Mechanics* 54 (2) (2022) 414–424.
- [54] R. Au-Yeung, A. Williams, V. Kendon, S. Lind, Quantum algorithm for smoothed particle hydrodynamics, *Computer Physics Communications* 294 (2024) 108909.
- [55] Y. D. Li, C. F. Wang, Y. Li, P. Joli, M. B. Liu, Z. Q. Feng, A coupled stabilized scheme on decoupled finite smoothed particle hydrodynamics and distributed contact discrete element method to simulate fluid-rigid-body interaction with multibody contacts, *Ocean Engineering* 316 (2025) 119962.

- [56] T. John, R. Poole, A. Kowalski, C. Fonte, A comparison between the fene-p and sppt constitutive models in large-amplitude oscillatory shear, *Journal of Fluid Mechanics* 979 (2024) A10.
- [57] J. King, S. Lind, High weissenberg number simulations with incompressible smoothed particle hydrodynamics and the log-conformation formulation, *Journal of Non-Newtonian Fluid Mechanics* 293 (2021) 104556.
- [58] R. Fattal, R. Kupferman, Constitutive laws for the matrix-logarithm of the conformation tensor, *Journal of Non-Newtonian Fluid Mechanics* 123 (2) (2004) 281–285.
- [59] R. Fattal, R. Kupferman, Time-dependent simulation of viscoelastic flows at high weissenberg number using the log-conformation representation, *Journal of Non-Newtonian Fluid Mechanics* 126 (1) (2005) 23–37.
- [60] M. A. Hulsen, R. Fattal, R. Kupferman, Flow of viscoelastic fluids past a cylinder at high weissenberg number: Stabilized simulations using matrix logarithms, *Journal of Non-Newtonian Fluid Mechanics* 127 (1) (2005) 27–39.
- [61] J. López-Herrera, S. Popinet, A. Castrejón-Pita, An adaptive solver for viscoelastic incompressible two-phase problems applied to the study of the splashing of weakly viscoelastic droplets, *Journal of Non-Newtonian Fluid Mechanics* 264 (2019) 144–158.
- [62] R. Comminal, J. Spangenberg, J. H. Hattel, Robust simulations of viscoelastic flows at high weissenberg numbers with the streamfunction/log-conformation formulation, *Journal of Non-Newtonian Fluid Mechanics* 223 (2015) 37–61.
- [63] K. Ghosh, Encoding classical data into a quantum computer (2021). [arXiv:2107.09155](https://arxiv.org/abs/2107.09155).
- [64] I. F. Araujo, D. K. Park, T. B. Ludermir, W. R. Oliveira, F. Petruccione, A. J. Da Silva, Configurable sublinear circuits for quantum state preparation, *Quantum Information Processing* 22 (2023) 123.
- [65] K. Chen, J. Liu, F. Yan, Exploring quantum neural networks for binary classification on mnist dataset: A swap test approach, *Neural Networks* 188 (2025) 107442.
- [66] X. Huang, W. Zhang, S. Zhang, Practical quantum protocols for blind millionaires’ problem based on rotation encryption and swap test, *Physica A: Statistical Mechanics and its Applications* 637 (2024) 129614.
- [67] J. Zhao, Y. H. Zhang, C. P. Shao, Y. C. Wu, G. C. Guo, G. P. Guo, Building quantum neural networks based on a swap test, *Physical Review A* 100 (1) (JUL 23 2019).
- [68] S. Balakrishnan, R. Sankaranarayanan, Operator-schmidt decomposition and the geometrical edges of two-qubit gates, *Quantum Information Processing* 10 (4) (2011) 449–461.
- [69] P. W. Shor, Polynomial-time algorithms for prime factorization and discrete logarithms on a quantum computer, *SIAM Journal on Computing* 26 (5) (1997) 1484–1509.
- [70] Y. D. Li, Y. Li, C. F. Wang, P. Joli, Z. Q. Feng, Numerical investigation on a comprehensive high-order finite particle scheme, *Applied Mathematics and Mechanics-English Edition* 46 (6) (2025) 1187–1214.
- [71] R. Fatehi, M. T. Manzari, Error estimation in smoothed particle hydrodynamics and a new scheme for second derivatives, *Computers & Mathematics with Applications* 61 (2) (2011) 482–498.
- [72] X. Y. Xu, L. Y. Tian, S. Peng, P. Yu, Development of sph for simulation of non-isothermal viscoelastic free surface flows with application to injection molding, *Applied Mathematical Modelling* 104 (2022) 782–805.
- [73] D. Rajagopalan, R. C. Armstrong, R. A. Brown, Finite element methods for calculation of steady, viscoelastic flow using constitutive equations with a newtonian viscosity, *Journal of Non-Newtonian Fluid Mechanics* 36 (1990) 159–192.